

^{GA}SAKe : forecasting landslide activations by a Genetic-Algorithms based hydrological model

Oreste G. Terranova¹, Stefano Luigi Gariano^{2,3*}, Pasquale Iaquineta¹ & Giulio G.R. Iovine¹

¹) CNR-IRPI (National Research Council – Research Institute for Geo-Hydrological Protection),
via Cavour 6, 87036, Rende, Cosenza, Italia.

²) CNR-IRPI (National Research Council – Research Institute for Geo-Hydrological Protection),
via Madonna Alta 126, 06128, Perugia, Italia.

³) University of Perugia, Department of Physics and Geology, via A. Pascoli, 06123, Perugia,
Italia.

*Corresponding Author: gariano@irpi.cnr.it, Phone: +39 075 5014424.

ABSTRACT

^{GA}SAKe is a new hydrological model aimed at forecasting the triggering of landslides. The model is based on Genetic Algorithms and allows to obtain thresholds for the prediction of slope failures using dates of landslide activations and rainfall series. It can be applied to either single landslides or set of similar slope movements in a homogeneous environment.

Calibration of the model provides families of optimal, discretized solutions (kernels) that maximize the fitness function. Starting from the kernels, the corresponding mobility functions (i.e., the predictive tools) can be obtained through convolution with the rain series. The base time of the kernel is related to the magnitude of the considered slope movement, as well as to the hydro-geological complexity of the site. Generally, shorter base times are expected for shallow slope instabilities compared to larger-scale phenomena. Once validated, the model can be applied to estimate the timing of future landslide activations in the same study area, by employing measured or forecasted rainfall series.

Examples of application of ^{GA}SAKe to a medium-size slope movement (the Uncino landslide at San Fili, in Calabria, Southern Italy) and to a set of shallow landslides (in the Sorrento Peninsula, Campania, Southern Italy) are discussed. In both cases, a successful calibration of the model has been achieved, despite unavoidable uncertainties concerning the dates of occurrence of the slope movements. In particular, for the Sorrento Peninsula case, a fitness of 0.81 has been obtained by calibrating the model against 10 dates of landslide activation; in the Uncino case, a fitness of 1 (i.e., neither missing nor false alarms) has been achieved using 5 activations. As for temporal validation, the experiments performed by considering further dates of activation have also proved satisfactory. In view of early-warning applications for civil protection, the capability of the model to simulate the occurrences of the Uncino landslide has been tested by means of a progressive, self-adaptive procedure. Finally, a sensitivity analysis has been performed by taking into account the main parameters of the model.

The obtained results are quite promising, given the high performance of the model against different types of slope instabilities characterized by several historical activations. Nevertheless, further refinements are still needed for application to landslide risk mitigation within early-warning and decision-support systems.

Key words: hydrological model, rainfall threshold, landslide triggering, genetic algorithm

46 1 INTRODUCTION

47 A nationwide investigation, carried out by the National Geological Survey, identified approximately
48 5×10^5 slope movements in Italy, with an average of 1.6 failures per square kilometre (Trigila,
49 2007). According to other investigations, this figure would rather be a low estimate (cf. Servizio
50 Geologico, Sismico dei Suoli, 1999; Guzzetti et al., 2008). In the period 1950–2009, at least 6349
51 persons were killed, went missing, or were injured by landslides, with an average of 16 harmful
52 events per year, thus confirming the notable risk posed to population (Guzzetti, 2000; Salvati et al.,
53 2010).

54 Petley (2008) estimated that about 90% of worldwide casualties can be attributed to landslides
55 triggered by rainfall. With reference to the Italian territory, about 70% of landslides result to be
56 triggered by rainfall (cf. CNR-GNDCI AVI Project, Alfieri et al., 2012). Slope instability conditions
57 are in fact influenced by rainfall that, infiltrating into the slopes, cause temporary changes in
58 groundwater dynamics (Van Asch et al., 1999). The combination of infiltration and runoff may
59 cause different types of mass-movements (either slope failure or erosion processes) depending on
60 the intensity and duration of the rainfall and the values of soil suction (Cuomo and Della Sala,
61 2013). Concentration of water deriving from either contemporary or antecedent storms at specific
62 sites plays a major role in triggering landslides – as testified by slope instabilities that commonly
63 follow the heaviest phases of rainfall events.

64 To model the relationships between rainfall and landslide occurrence, two distinct approaches are
65 generally adopted in literature. The first, named “complete” or “physically-based”, attempts to
66 determine the influence of rainfall on slope stability by modelling its effects in terms of overland
67 flow, groundwater infiltration, pore pressure and related balance of shear stress and resistance (cf.
68 e.g., Montgomery and Dietrich, 1994; Wilson and Wieczorek, 1995; Crosta, 1998; Terlien, 1998;
69 Crosta et al., 2003; Pisani et al., 2010). With regard to this latter purpose, numerical models are
70 employed, and a notable (and expensive) amount of detailed data is commonly required to define
71 the geological scheme of the slope in litho-structural, hydrogeological, morphologic and
72 geotechnical terms. The second approach (adopted in the present study), named “empirical” or
73 “hydrological” (Cascini and Versace, 1988), is based on a statistical-probabilistic analysis of
74 rainfall series and of dates of occurrence of slope movements (see, among the others, Campbell,
75 1975; Caine, 1980; UNDRO, 1991; Sirangelo and Versace, 1996; Guzzetti et al., 2007; 2008,
76 Brunetti et al. 2010, Gariano et al., 2015). In literature, methodological examples generally focus on
77 thresholds obtained for *i*) single phenomena or *ii*) given types of landslides within a homogeneous
78 geo-environmental setting (cf. e.g., Jakob and Weatherly, 2003).

79 In this study, the hydrological model ^{GA}SAKe (i.e., the Genetic-Algorithms based release of the
80 model Self Adaptive Kernel), developed to forecast the triggering of slope movements, is described.
81 The model can be applied to either single landslides or to a set of similar phenomena within a
82 homogeneous study area. Model calibration is performed by means of Genetic Algorithms: in this
83 way, a family of optimal, discretized kernels can iteratively be obtained from initial tentative
84 solutions. In a different release of the model (^{CM}SAKe – i.e., *Cluster model SAKe*) the calibration is
85 instead performed through an iterative procedure (Terranova et al., 2013).

86 Examples of application of the model to a medium-size landslide (the Uncino landslide at San Fili)
87 and to shallow slope movements in the Sorrento Peninsula are discussed in the following sections.
88 Temporal validation is discussed for both cases, in view of early-warning applications of ^{GA}SAKe
89 for Civil Protection purposes. Moreover, a progressive, self-adaptive procedure of calibration and
90 validation is discussed, by considering the Uncino case study, to verify changes in fitness,

91 predictive ability and base time when an increasing number of dates of activation is employed.
92 Finally, the results of preliminary, parametric analyses are presented, aimed at investigating the role
93 of the main parameters of the model.

94

95 **2 BACKGROUND**

96 Physical systems evolve in time due to their own inner dynamics and/or as a consequence of
97 external causes. Suitable observational tools can be employed to monitor their evolution, and
98 arranged to promptly send reports or warnings to authorities of civil protection to support the
99 management of emergencies (Cauvin et al., 1998; for applications to landslides, cf. also Keefer et
100 al., 1987; Iovine et al., 2009; Capparelli and Versace, 2011; Pradhan and Buchroithner, 2012).

101 In the case of complex systems (e.g., nuclear power stations, telecommunication networks, etc.),
102 many parameters, in part interdependent, have to be monitored. Missing an automated phase of
103 analysis and proper filtering, a great number of reports may be delivered by the monitoring
104 apparatus in few seconds. At this purpose, the concepts of threshold (Carter, 2010), event and
105 warning must therefore be suitably defined.

106 Regarding slope movements, the notions of threshold and warning have long been investigated. In
107 particular, a threshold constitutes a condition - generally expressed in quantitative terms or through
108 a mathematical law - whose occurrence implies a change of state (White et al., 1996). According to
109 the ALARM study group (Cauvin et al., 1998), an event is *i*) a portion of information extracted
110 from either continuous or discrete signals (i.e., a significant variation), transmitted by a component
111 of the monitoring network; or *ii*) a set of data concerning the considered context (e.g., restorations,
112 actions, observations). According to such definition, an event must be instantaneous and dated. As
113 for warning, its definition derives from that of event: it is a discrete indicator aimed at triggering a
114 human or an automated reaction. The warning can be classified into distinct levels (e.g., in terms of
115 security) or by type (e.g., related to a distinct component of the dynamic system under
116 consideration), to be transmitted by the monitoring system.

117 In complex systems, causal factors responsible for emergency conditions may be difficult to
118 identify. Therefore, warnings may be issued according to pre-fixed thresholds related to suitable
119 physical properties of the system. In these cases, the timing of data sampling of the monitoring
120 instruments should be progressively adapted to the evolution of the phenomenon. A further issue
121 concerns the chances of missing and false alarms, as well as the camouflage of an alarm among
122 simultaneous others.

123 In physical terms, slope instability can occur when the shear strength gets lower than a given
124 threshold (Terzaghi, 1962). Rain infiltration may temporarily change the dynamics of groundwater
125 (Van Asch et al., 1999): due to an increase in pore water pressure, the effective shear strength of the
126 material decreases, and a slope movement can be triggered. Groundwater may reach a given
127 location within the slope by different paths. The main natural mechanisms include: *i*) surface flow,
128 strongly influenced by morphology; *ii*) direct infiltration from the surface; *iii*) flow within the soil
129 mantle (*throughflow*) from upslope and sideslopes; *iv*) seepage from the bedrock toward the
130 overlying colluvium. The length of the different paths may be quite different, and characterized by
131 distinct velocities: as a consequence, aliquots of the same rainfall event may reach a given site at
132 different times, variously combining with other groundwater amounts (Ellen, 1988).

133 To apply a hydrological approach, empirical relations have to be determined by means of thresholds
134 to distinguish among conditions which likely correspond to landslide occurrence or not. To this
135 aim, different hydrological parameters can be selected (Guzzetti et al., 2007; 2008 and

136 <http://rainfallthresholds.irpi.cnr.it/>): the cumulative rain recorded in a given temporal window
137 (hours/days/months) before landslide activation; the average rain intensity in the same temporal
138 window; rains normalized to reference values (e.g., annual averages). Simplified hydrological
139 balances can also be adopted in empirical approaches, by considering losses of aliquots of rains by
140 run-off, evapo-transpiration, etc.

141 As concerns superficial landslides, triggering thresholds can be derived from relations between the
142 “triggering” rain (daily, hourly or shorter), corresponding to the onset of the slope movement, and
143 the rain cumulated over an “antecedent period” (usually, few days to two weeks before landslide
144 activation) (e.g., Campbell, 1975; Cannon and Ellen, 1985; Wieczorek, 1987; Terlien, 1996; Crosta,
145 1998; Zêzere and Rodrigues, 2002). In other cases, thresholds refer to relations between rain
146 intensity, I , and duration, D (e.g., Brunetti et al., 2010, Berti et al., 2012, Peres and Cancelliere,
147 2014). In some studies, antecedent rains are also considered, allowing to obtain better results (e.g.,
148 Campbell, 1975). Larger amounts of antecedent rain should allow slope movements to be activated
149 by less severe triggering storms. In general, a direct relationship between antecedent rain and
150 landslide dimension can be observed (Cascini and Versace, 1986); though, in some peculiar
151 conditions (e.g., Hong Kong case studies, caused by suction reduction - Brand et al., 1984) this is
152 not the case, and the role of antecedent rains looks less important. In addition, as underlined by
153 Cuomo and Della Sala (2013), time to runoff, time to failure and runoff rates strongly depend on
154 soil water characteristic curves, soil initial conditions, rainfall intensity and slope angle in
155 unsaturated shallow deposits. Moreover, soil mechanical parameters affect the time to failure,
156 which can result either shorter or longer than time to runoff.

157 Due to physical and economic issues, difficulties in hydrological modelling of landslides generally
158 increase when dealing with deeper and larger phenomena (Cascini and Versace, 1986). In such
159 cases, landslide activation depends on the dynamics of deeper groundwater bodies. By the way, it is
160 not by chance that most studies do refer to small and superficial slope movements. Large landslides
161 usually show complex relationships with rains, as different groundwater aliquots may combine and
162 reach the site of triggering. Depending on type (cf. dimension, material, kinematics, etc.), different
163 hydrological mechanisms should be considered, thus limiting the possibility of generalization of the
164 thresholds (Dikau and Schrott, 1999; Corominas, 2001; Marques et al., 2008). Again, the
165 mobilization of deeper phenomena commonly requires greater rainfall amounts, spanned over
166 longer periods, with respect to shallow landslides (Aleotti, 2004; Terranova et al., 2004; Guzzetti et
167 al., 2007; 2008;). In these cases, rain durations responsible for landslide activations commonly
168 range from ca. 30 days to several months, even beyond a single rainy season (Brunsdon, 1984; Van
169 Asch et al., 1999; Gullà et al., 2004; Trigo et al., 2005).

170 To analyse the triggering conditions of slope movements – either shallow or deep-seated – a
171 threshold-based modelling approach can be employed. Empirical thresholds (e.g., Aleotti, 2004;
172 Wieczorek and Glade, 2005; Terranova et al., 2004; Vennari et al., 2014) can be expressed in terms
173 of curves, delimiting the portion of the Cartesian plane which contains “all and only” the
174 hydrological conditions related to known activations (cf. e.g., the I - D chart proposed by Caine,
175 1980). A further improvement to this approach can be obtained by considering hydrological
176 conditions not related to landslide activations (Crozier, 1997; Sengupta et al., 2010; Gariano et al.,
177 2015). In general, no changes of state are assumed to occur below the threshold (z_t), while they do
178 happen above it. Alternatively, a range of conditions can be defined (Crozier, 1997), delimited by:
179 ✓ a lower threshold (z_{low}), below which changes of state do never occur, and
180 ✓ an upper threshold (z_{upp}), above which changes always happen.

181 For values between z_{upp} and z_{low} , the probability that the state changes can be defined, essentially
 182 depending on *i*) the incompleteness of knowledge on the physical process under investigation, and
 183 *ii*) the incapacity of the model to fully replicate the behaviour of the same process. In probabilistic
 184 terms:

$$\begin{aligned}
 P(E_t) &= 0 \text{ for } z(t) < z_{low} \\
 P(E_t) &= 1 \text{ for } z(t) > z_{upp} \\
 P(E_t) &= G[z(t)] \text{ for } z_{low} \leq z(t) \leq z_{upp}
 \end{aligned} \tag{1}$$

185 in which: P is the probability of occurrence (1=success, 0=unsuccess); E_t is a process (succession of
 186 events) whose state changes with time t ; $z(t)$ is the value assumed, at time t , by the variable that
 187 determines the change of state; z_{low} and z_{upp} are the minimum and maximum thresholds,
 188 respectively; $G[z(t)]$ is a probability function, monotonically increasing with t in the range $]0,1[$.
 189 In hydrological models, to express the influence of rainfall on runoff and groundwater dynamics, a
 190 “kernel” (also named “filter function”) can be employed, usually defined in terms of simple,
 191 continuous analytical function (Chow et al., 1988). In such a way, suitable weights can be assigned
 192 to the precipitations occurred in the last hours/days before a given geo-hydrological process (e.g.,
 193 discharge, measured at a generic river cross section; landslide activation), as well as to earlier rains
 194 recorded weeks/months before. The mostly employed types of kernels are Beta, Gamma, Nash,
 195 negative exponential distribution. Furthermore, the “base time” (t_b) expresses a sort of memory with
 196 respect to rainfall: in classic rainfall-runoff modelling, t_b defines the time of concentration, while in
 197 slope stability analyses it represents the time interval, measured backward from landslide activation,
 198 during which rainfall is deemed to effectively affect groundwater dynamics, and contributes to
 199 destabilization.

200 To modelling slope stability, both the shape and the base time of the kernel must be properly
 201 selected depending on type and dimension of the investigated phenomena, as well as geo-structural
 202 and hydrogeological characteristics. Unfortunately, in several real cases, the above-mentioned
 203 analytical functions may fail in properly capturing the complexity of groundwater dynamics, as well
 204 as the related landslide activations. In this respect, the adoption of discretized kernels, automatically
 205 calibrated through iterative computational techniques, may offer effective solutions.

207 **3 THE MODEL ^{GA}SAKe**

208 ^{GA}SAKe is an empirical-hydrological model for predicting the activation of slope movements of
 209 different types. It is based on a classic threshold scheme: the exceedance of the threshold
 210 determines a change of state, i.e. the triggering of the landslide. The scheme is inspired from the
 211 *FLaIR* model (*F*orecasting *L*andslides *I*nduced by *R*ainfall), proposed by Sirangelo and Versace
 212 (1996): through changes of state in time, the variable $z(t)$ assumes the meaning of “*mobility*
 213 *function*”. In other terms, the values of $z(t)$ depend on the amount of rain stored in the aquifer.
 214 In hydrology, rainfall-runoff modelling is commonly performed by adopting a linear, steady scheme
 215 (Chow et al., 1988). Such approach implies that the transformation of rainfall in runoff can be
 216 described by an integral of convolution between a unitary impulsive response of the basin – the
 217 kernel, $h(t)$ – and the rainfall, $p(t)$.

218 The *kernel (filter function)* represents the unitary volume influx in an infinitesimal period, and is
 219 defined as:

$$\int_0^{\infty} h(t)dt = 1 \tag{2}$$

220 in which $h(t)=h(-t)$, $h(t) \geq 0$, $\forall t$.

221 In practical applications, the lower bound ($t=0$) corresponds to the beginning of the flood-wave
222 rising, and the kernel assumes a finite duration (t_b). The integral of convolution is therefore
223 expressed as:

$$z(t) = \int_0^{t_b} h(t - \tau) p(\tau) d\tau = \int_0^{t_b} h(\tau) p(t - \tau) d\tau \quad (3)$$

224 in which $z(t)$ represents the discharge at the time t . For a specific case study, the kernel can be
225 determined by means of calibration procedures, by relating discharge measurements to rains.

226 In discretized terms, the elements of the kernel are characterized by width Δt and height h_i , and
227 equation (3) can be written as:

$$z_u = \sum_{i=1}^u h_i \cdot p_{u-i+1} \cdot \Delta t \quad (4)$$

228
229 Sirangelo and Versace (1996) proved that the same approach may turn out promising also in slope-
230 stability modelling. Capparelli and Versace (2011) stressed that the *I-D* chart of Caine (1980)
231 corresponds to a kernel defined by a power function $h(t) = a t^b$, with $b < 0$. Exporting the well-
232 established knowledge of rainfall-runoff modelling (usually based on many measurements) to
233 rainfall-landslide modelling is not trivial, due to scarcity of adequate information for proper
234 calibration. Only few dates of activation are, in fact, commonly available in rainfall-landslide
235 modelling (often with unsatisfactory details on location and phenomena), and the values of $z(t)$ are
236 unknown. From a mathematical point of view, such a problem can be handled by assuming that the
237 timing of the maxima of $z(t)$ corresponds to the dates of landslide activation. When studying the
238 triggering conditions of landslides, calibration can be therefore performed by maximizing the
239 mobility function in correspondence to the dates of activation.

240 Scarcity of information inevitably reflects on the resulting kernel, whose shape may turn out highly
241 indeterminate: different functions, or different parameters of the same function, can in fact
242 maximize $z(t)$ in correspondence to the dates of mobilization. Model optimization – and its reliable
243 utilization for early-warning purposes – can turn out an awkward issue.

244 In this work, an innovative modelling approach – based on discretized kernels, automatically
245 calibrated through iterative computational techniques – is proposed, which may help in facing the
246 above-cited difficulties. For modelling purposes, the rainfall series and a coherent set of dates of
247 landslide occurrence – either related to a given slope movement, or to a set of landslides of the same
248 type in a homogeneous geo-environmental zone – must be given as input.

249 Unfortunately, when dealing with the timing of occurrence, historical notices may refer either to
250 portions of the considered phenomena or to entire landslide bodies. Therefore, dates should be
251 properly selected to consider only consistent cases. Moreover, dates of activation are usually known
252 with only a broad approximation: with respect to the reports, the actual timing of occurrence may be
253 located backward (documents may assign a later date) or forward (in case of later, more relevant
254 movements). For modelling purposes, it is then useful to specify a temporal window, lasting from
255 an initial (d_{t-from}) to a final date (d_{t-to}), containing the presumable timing of occurrence.

256 Rainfall series are commonly reconstructed from data recorded at rain gauges located within a
257 reasonable proximity of the study site. The temporal window of the hydrological analysis is defined
258 by the intersection of *i*) the period of observation of the rains and *ii*) the period delimited by the
259 ancientmost and the recentmost dates of activation of the landslide. A potential source of

260 uncertainty lies in the fact that, occasionally, the recorded rainfall amounts notably differ from those
261 actually experienced at landslide location. Furthermore, landslide triggering may also be due to
262 other causes (e.g., human activity, earthquakes): a thorough preliminary analysis has always to be
263 performed to verify the significance of rainfall preceding landslide activation, to detecting cases not
264 to be considered in the hydrological study.

265 In the model, rains older than t_b are neglected. Suitable maximum and minimum values (t_{b-max} and
266 t_{b-min}) have to be initialized to allow the model to determine optimal values. Commonly, t_b ranging
267 from few hours to some weeks are suggested for shallow landslides, while greater values (up to
268 several months) sound suitable for deep-seated phenomena.

269 Based on the geological knowledge of the phenomenon under investigation, the initial shape of the
270 kernel can be assumed among a set of basic types. Among these, *i*) a “rectangular” shape can be
271 adopted if older precipitations have the same weight of more recent rains; *ii*) a “decreasing
272 triangular”, if older precipitations have a progressively smaller weight than more recent rains; *iii*)
273 “increasing triangular”, if older precipitations have a progressively greater weight than more recent
274 rains. A casual shape or any other function can also be implemented in the model (e.g., Beta,
275 Gamma, Nash, Negative exponential distribution).

276

277 **3.1 Model Calibration**

278 In GA SAKe, model calibration is performed against real case studies through Genetic Algorithms
279 (GAs). These latter are general-purpose, iterative search algorithms inspired by natural selection
280 and genetics (Holland, 1975). Since 1970’s, GAs have been applied to several fields of research,
281 from applied mathematics (Poon and Sparks, 1992), to evolution of learning (Hinton and Nowlan,
282 1987), evolutionary robotics (Nolfi and Marocco, 2001), and debris-flow modelling (Iovine et al.,
283 2005; D’Ambrosio et al., 2006). GAs simulate the evolution of a population of candidate solutions
284 to a given problem by favouring the reproduction of the best individuals. The candidate solutions
285 are codified by genotypes, typically using strings, whose elements are called genes.

286 GAs explore the solution space, defined as the set of possible values of the genes. At the beginning
287 of a given optimization experiment, the members of the initial population of genotypes (in this
288 study, the *kernels*) are usually generated at random. The performance of each solution, in terms of
289 phenotype (i.e., the *mobility function*), is evaluated by applying a suitable *fitness function*, so
290 determining its “adaptability”, i.e. the measure of its goodness in resolving the problem.

291 The sequence of random genetic operators *selection*, *crossover* and *mutation*, constrained by
292 prefixed probabilities, constitutes a single GA-iteration that generates a new population of candidate
293 solutions. At each iteration, best individuals are in fact chosen by applying the selection operator.

294 To form a new population of offspring, crossover is employed by combining parents’ genes.

295 Mutation is successively applied to each gene, by randomly changing its value within the allowed
296 range. Thanks to the GA approach, better individuals (i.e., those characterized by higher fitness
297 values) can be obtained over time. In fact, according to individual probabilities of selection, any
298 change that increases the fitness tends to be preserved over GA iterations (Holland, 1975). For
299 further details on GAs, cf. Goldberg (1989) and Mitchell (1996).

300 In the present study, a steady-state and elitist GA (cf. De Jong, 1975) was employed to obtain the
301 family of optimal kernels that maximize the mobility function in correspondence to known dates of
302 landslide activations. The procedure employed for calibration of GA SAKe is schematized in Figure 1.
303 At the beginning of an optimization experiment, the initial population of N kernels is generated at
304 random, and the fitness of the related mobility functions is evaluated (cf. below). In order to evolve

305 the initial population of candidate solutions, and to progressively obtain better solutions, a total
 306 number of A GA-iterations follows.

307 At each iteration of the GA, the operators selection, crossover and mutation are applied as follows
 308 (Fig. 2):

309 • *selection*

310 *i.* n_e “elitist” individuals are merely copied in a “mating pool” from the previous generation, by
 311 choosing the best ones;

312 *ii.* the remaining $N-n_e$ candidate solutions are chosen by applying the “*tournament without*
 313 *replacement*” selection operator. More in detail, a series of tournaments are performed by
 314 selecting two individuals at random from the previous generation: the winner (i.e., the one
 315 characterized by the highest fitness) is copied into the mating pool, according to a prefixed
 316 surviving probability (p_s), which is set greater for the fittest individual. Note that, when
 317 choosing the $N-n_e$ candidate solutions, a given individual cannot be selected more than once.

318 • *crossover*

319 After the mating pool is filled with N individuals, the crossover operator is applied, according to
 320 a prefixed probability (p_c):

321 *i.* two parent individuals are chosen from the mating pool at random;

322 *ii.* a cutting point (*crossover point*) is then selected at random in the range $]t_{b-min}, t_{b-max}[$;

323 *iii.* the obtained portions of parents’ strings are exchanged, thus mixing the genetic information
 324 and resulting in two children (Fig. 3).

325 When the crossover is not applied, the two parents are merely copied into P_{new} .

326 • *mutation*

327 Based on a prefixed probability (p_m), a random number of elements of the kernel (p_{me} , expressed
 328 as a percentage of t_b) is mutated, by adding to each element an amount dh that is randomly
 329 obtained in the range $[p_{mh1}, p_{mh2}]$, as a function of the maximum value of the kernel (h_{max}). Then
 330 dh ranges from dh_1 to dh_2 :

$$\begin{aligned} dh_1 &= p_{mh1} \cdot h_{max} \\ dh_2 &= p_{mh2} \cdot h_{max} \end{aligned} \quad (5)$$

331 Furthermore, the base time is also mutated (increased or decreased) within the bounds $[t_{b-min}, t_{b-}$
 332 $max]$, according to a random factor dt_b selected in the range $[1/p_{mtb}, p_{mtb}]$ (Fig. 4).

333 Children obtained by either crossover or mutation must be normalized before being included in the
 334 population P_{new} , by properly scaling the elements of the kernels to ensure validity of equation 2.

335 During calibration, the shape of the kernel and its t_b are iteratively refined. Note that the shape is not
 336 subject to any constraint, while t_b is allowed to vary in the range $[t_{b-min} - t_{b-max}]$. The fitness is
 337 computed for each examined mobility function, and new populations of kernels are generated as
 338 described above.

339 As for the fitness function, in ^{GA}*SAKe* it is defined as follows:

340 • the L available dates of landslide activation – as derived from the historical analyses – are
 341 arranged in a vector $\mathbf{S} = \{S_1, S_2, \dots, S_i, \dots, S_L\}$;

342 • the vector of the relative maxima of the mobility function, $\mathbf{Z} = \{z_1, z_2, \dots, z_j, \dots, z_M\}$, is sorted
 343 in decreasing order (M = number of relative maxima);

344 • the vector of the partial fitness is $\boldsymbol{\varphi} = \{\varphi_1, \varphi_2, \dots, \varphi_i, \dots, \varphi_L\}$, where $\varphi_i = k^{-l}$ depends on the rank k
 345 of the relative maxima of z_j that coincide with known dates of activation, S_i . In case S_i does not
 346 correspond to any relative maximum, it is $\varphi_i = 0$.

347 With reference to a given kernel, the resulting fitness is expressed by $\Phi_u = \sum_{i=1}^L \varphi_i$. To generalize
348 the results for an easier comparison with other study cases, a normalized fitness index is adopted, Φ
349 $= \Phi_u / \Phi_{max}$, defined in the range [0,1], being $\Phi_{max} = \sum_{i=1}^L 1/i$.

350 For instance, if two dates of activation are available and both are well captured by the mobility
351 function (i.e., they correspond to the highest peaks), the obtained fitness is $\Phi_u = 1 + 1/2 = 1.5$. On the
352 other hand, in case only one of the dates is captured and the remaining one ranks fifth, $\Phi_u = 1 + 1/5$
353 $= 1.2$.

354 Thanks to the above procedure, a family of “optimal kernels” which maximizes the fitness can be
355 determined. The mobility function is, in fact, forced toward a shape characterized by relative
356 maxima (z_j) coinciding with the dates of landslide occurrence (S_i). An optimal solution leads to a
357 mobility function having the highest peaks in correspondence to such dates; further peaks may also
358 be present, characterized by lower values. Nevertheless, kernel solutions generally determine
359 mobility functions whose highest peaks only partly match with the dates of landslide occurrence
360 (i.e., some dates may neither correspond to the highest peaks nor to any peak at all).

361 To select the most suitable kernel from a given family of optimal ones, let’s define:

- 362 • z_{j-min} as the lowest of the peaks of the mobility function in correspondence to one of the dates of
363 activation (S_i);
364 • z_{cr} as the “critical threshold”, i.e. the highest peak of the mobility function just below z_{j-min} ;
365 • the “safety margin”, $\Delta z_{cr} = (z_{j-min} - z_{cr}) / z_{j-min}$.

366 When applying the fitness function to evaluate a given kernel, either incompleteness or low
367 accuracy of input data may lead to “false alarms” – i.e., peaks of the mobility function (z_j) which are
368 greater than the threshold z_{cr} , but do not correspond to any of the known dates of activation. Such
369 alarms can actually be of two different types: 1) “untrue false”, due to an informative gap in the
370 archive (i.e., correct prediction); 2) “true false”, in case of real misprediction of the model. On such
371 cases, further historical investigations may help to discriminating between the mentioned types of
372 false alarms.

373 Also depending on the specific purpose of the analysis, the most suitable kernel can therefore be
374 selected by one or more of the following criteria: *i*) the greatest Δz_{cr} ; *ii*) the shortest t_b ; *iii*) the
375 smallest $\mu_0 = \sum_{i \leq t_b} (i - 0.5) h_i \Delta t$, i.e. the first-order momentum of the kernel with respect to the
376 vertical axis. The first criterion allows for the activation of early-warning procedures with greatest
377 advance; the remaining ones (to be employed when Δz_{cr} is too small) generally correspond to more
378 impulsive responses to rainfall.

379 Differently from what usually experienced in rainfall-runoff models, ^{GA}SAKe therefore provide
380 multiple equivalent solutions – i.e., a number of optimal kernels with same fitness, Φ_u , despite
381 different shapes. This may depend on the limited number of available dates of activations, and on
382 other noises in input data (e.g., rain gauges located too far from the site of landslide activation;
383 inaccurate information on dates of activation or on the phenomenon). The adoption of synthetic
384 kernels – e.g., obtained by averaging a suitable set of optimal kernels – permits to synthesize the
385 family of results for successive practical applications: in this work, the best 100 kernels obtained for
386 each case study were in fact utilized to synthesize “average kernels” (see below) to be employed for
387 validation purposes.

388

389 4 CASE STUDIES

390 The case studies considered in this paper are: *i*) a set of shallow landslides in the Sorrento Peninsula
391 between Gragnano and Castellammare di Stabia (Campania, Southern Italy); and *ii*) the Uncino
392 landslide at San Fili (Calabria, Southern Italy).

393 Note that, as the numbers of known historical activations in the study areas were adequate, some
394 dates could be excluded from calibration, and were successively employed for validation purposes.
395 In particular, the recentmost dates of landslide activation (cf. Tables 1 and 2) were employed to
396 validate the average kernels (these latter obtained from the families of optimal solutions defined
397 through calibration). The procedure employed for validation is schematized in Figure 5.

398

399 **4.1 Shallow landslides in the Sorrento Peninsula - Campania**

400 The Sorrento Peninsula is located in western Campania, Southern Italy (Fig. 6). In the area,
401 Mesozoic limestone mainly crop out, covered by Miocene flysch, Pleistocene volcanic deposits
402 (pyroclastic fall, ignimbrite), and Pleistocene detrital-alluvial deposits (Di Crescenzo and Santo,
403 1999). The carbonate bedrock constitutes a monocline, gently dipping towards WNW, mantled by
404 sedimentary and volcanoclastic deposits, with thickness ranging from few decimetres to tens of
405 meters.

406 Rainfall-induced shallow landslides are widespread in the pyroclastic soils covering the slopes of
407 the study area. Among the various factors affecting the spatial distribution and the type of slope
408 instabilities, Cascini et al. (2014) pointed out that both the rainfall conditions and the consequent
409 seasonal variations of soil suction play a significant role. In particular, when suction is low and
410 frontal rainfall occurs (from November to May), first time shallow landslides are triggered; when
411 suction is high or very high and convective or hurricane-type rainfall occurs (from June to October),
412 mostly erosion phenomena occur, often turning into hyperconcentrated flows.

413 The study area is characterized by hot, dry summers and moderately cold and rainy winters.
414 Consequently, its climate can be classified as Mediterranean (Csa in the Köppen-Geiger's
415 classification). In particular, the mean annual temperature ranges from 8-9°C, at the highest
416 elevations of M. Faito and M. Cerreto, to 17-18°C along coasts and valleys. Average annual rainfall
417 varies from 900 mm west of Sorrento to 1500 mm at M. Faito; moving inland to the East, it reaches
418 1600 mm at M. Cerreto and 1700 mm at the Chiunzi pass (Ducci and Tranfaglia, 2005). On
419 average, annual totals are concentrated in about 95 rainy days. During the driest six months (from
420 April to September), only 30% of the annual rainfall is recorded in about 30 rainy days. During the
421 three wettest months (November, October, and December), a similar amount is recorded in about 34
422 rainy days (Servizio Idrografico, 1948-1999). In the area, convective rainstorms may occur,
423 characterized by a very high intensity, at the beginning of the rainy season (from September to
424 October). In Autumn-Winter, either high intensity or long duration rainfall are usually recorded,
425 while uniformly distributed rains generally occur in Spring (Fiorillo and Wilson, 2004). As for
426 annual maxima of daily rainfall recorded at the sea level, the Amalfi coast (southern border of the
427 Sorrento Peninsula) is characterized by smaller values (59 mm) of average annual maxima of daily
428 rainfall than the Sorrento coast (86 mm), on the northern border. Such difference seems to persist
429 even at higher elevations (up to 1000 m a.s.l.), with 84 mm vs. 116 mm for the southern and
430 northern mountain slopes, respectively (Rossi and Villani, 1994).

431 Severe storms frequently affect the study area, triggering shallow landslides that propagate seaward,
432 often causing casualties and serious damage to urbanized areas and transportation facilities (Mele
433 and Del Prete, 1999; Calcaterra and Santo, 2004; Di Crescenzo and Santo, 2005). In the second half
434 of the XX century, several shallow landslides activated nearby Castellammare di Stabia: in Table 1,

435 the major events recorded between Vico Equense and Gragnano are listed, with details on types of
436 events, affected sites and references. Shallow landslides listed in Table 1 occurred between
437 November and March, a period characterised by a medium to low suction range and included in the
438 rainy season (October to April), according to Cascini et al. (2014). The same Authors pointed out
439 that, in this period, frontal rainfall typically occurs and may trigger widespread first-time shallow
440 landslides, later propagating as debris flow or debris avalanches.
441 Rainfall responsible for landslide occurrences in the Sorrento Peninsula are shown in Fig. 7, in
442 terms of cumulated antecedent rains, extracted from the records of the nearest gauges (Tramonti,
443 Castellammare, and Tramonti-Chiunzi – cf. Fig. 6). The trends of antecedent rains look quite
444 different, ranging from abrupt (cf. curves 5, 6, 7) to progressive increases (cf. 2, 4, 10). On the other
445 hand, the curve 0 does not highlight significant amounts of rainfall in the 14 days preceding
446 landslide activation: therefore, the occurrence recorded on 14 April 1967 was excluded by the
447 hydrological analysis. Quite moderate amounts of cases 6 and 7 (occurred on 4 November 1980 and
448 14 November 1982, resp.) were instead recorded in short periods, thus resulting into high-intensity
449 events that could be considered as triggering factor of the observed landslides.
450 As a result, the dates of activation from #1 to #10 were selected for calibration, whilst #11 was
451 employed for validation. As shallow landslides were being considered, the rainfall period employed
452 for calibration spanned from 17 January 1963 to 10 December 1996; for validation, the rainfall
453 series extended from 11 December 1996 to 10 February 1997 – i.e., to the validation date $+t_b$ (this
454 latter as obtained from calibration).

455 **4.2 The Uncino landslide - San Fili (Northern Calabria)**

457 San Fili (Fig. 8) is located on the western margin of the Crati *graben*, a tectonic depression along
458 the active Calabrian-Sicilian Rift Zone (Monaco and Tortorici, 2000). In the area, vicarious, N-S
459 trending normal faults mark the base of the Coastal Chain, at the transition between Palaeozoic
460 metamorphic rocks, to the West, and Pliocene-Quaternary sediments, to the East (Amodio Morelli
461 et al., 1976). Nearby San Fili, Palaeozoic migmatitic gneiss and biotitic schist, generally weathered,
462 are mantled by a Late Miocene sedimentary cover of reddish continental conglomerate, followed by
463 marine sandstone and clays (CASMEZ, 1967). In particular, the village lies in the intermediate
464 sector between two faults, marked by a NE-SW trending connection fault, delimiting Miocene
465 sediments, to the North, from gneissic rocks, to the South.

466 In Calabria, the Tyrrhenian sector (including the study area) results rainier than the Ionian (about
467 1200-2000 mm vs. 500 mm). Nevertheless, the most severe storms occur more frequently in the
468 Ionian sector (Terranova, 2004). The average annual temperature is about 15°C: the coldest months
469 are January and February (on average, 5°C), followed by December (8°C); the hottest months are
470 July and August (24°C), followed by June (22°C).

471 As in most of the region, the climate at San Fili is Mediterranean (Csa, according to Köppen, 1948).
472 Being located on the eastern side of a ridge, the area is subject to *Föhn* conditions with respect to
473 perturbations coming from the Tyrrhenian sea. It is characterized by heavy and frequent Winter
474 rainfall, caused by cold fronts mainly approaching from North-West, and Autumn rains, determined
475 by cold air masses from North-East. In Spring, rains show lower intensities than in Autumn, whilst
476 strong convective storms are common at the end of Summer. The average monthly rains recorded at
477 the Montalto Uffugo gauge (the closest to San Fili) are listed in Table 3. From October to March
478 (i.e., the wet semester), 77% of the annual rainfall is totalized in about 77 rainy days; 36% of the

479 annual rainfall is recorded in 38 days during the three wettest months; finally, from June to August
480 (i.e., the three driest months), 6% of the annual rains fall in 11 days.
481 The Uncino landslide is located at the western margin of San Fili (Fig. 8). It is a medium-size rock
482 slide (maximum width = 200 m, length > 650 m, estimated maximum vertical depth = 25 m), with a
483 deep-seatedness factor (sensu Hutchinson, 1995) that may be classified as “intermediate”. The slope
484 movement involves Late Miocene conglomerate, arenite and marly clay overlaying Palaeozoic
485 gneiss and biotitic schist. It repeatedly affected the village, damaging the railway and the local road
486 network, besides some buildings: the ancientmost known activation dates back to the beginning of
487 the XX Century (Sorriso-Valvo et al., 1996); from 1960 to 1990, seven dates of mobilization are
488 known (as listed in Table 2). On such events, the railroad connecting Cosenza to Paola was
489 damaged or even interrupted. By the way, on 28 April 1987, the railway was put out of service,
490 hence the relevance of the infrastructure decreased, together with media attention. Usually, such
491 type of information is collected from archives not compiled by landslide experts, and is therefore
492 affected by intrinsic uncertainty (e.g., concerning the dates of activity, and the partial or total
493 activation of the phenomenon), with unavoidable problems of homogeneity of the data employed
494 for model calibration.
495 The informative content of the Uncino case study is quite high, and allows for a more accurate
496 calibration of the kernel with respect to the Sorrento Peninsula case: consequently, a smaller family
497 of optimal solutions is expected. Nevertheless, the known activations still suffer from uncertainties
498 related to dates and affected volumes.
499 Cumulated antecedent rains, corresponding to the Uncino landslide occurrences, are shown in Fig.
500 9. Rainfall data were extracted from the records of the Montalto Uffugo rain gauge (cf. Fig. 8). The
501 trends of antecedent rains may be distinguished into 3 main patterns: the curve 2 shows a constant
502 increase of rainfall in time, totalizing the greatest amounts from ca. 90 to 180 days. On the other
503 hand, the case 0 shows the lowest values throughout the considered accumulation period. The
504 curves 1, 3, 4, and 5 totalize intermediate values, with abrupt increases from 120 to 180 days for
505 curves 3 and 5. Finally, the case 6 looks similar to case 2 between 30 and 90 days, but shows no
506 more increases in the remaining period (analogously to 1 and 4).
507 As the curve 0 does not highlight significant amounts of rainfall in the 30-180 days preceding the
508 landslide activation, the occurrence recorded on 23 November 1988 was excluded from the
509 hydrological analysis. Of the remaining curves, case 1 generally shows the lowest amounts from ca.
510 40 to 180 days. Consequently, the dates of activation from #1 to #5 were selected for calibration,
511 whilst #6 was employed for validation. Since a medium-size landslide was being considered, the
512 rainfall period employed for calibration spans from 1 September 1959 to 31 August 1980; for
513 validation, it ranges from 1 September 1980 to 31 March 1981 – i.e., including the validation date
514 by $\pm t_b$ (this latter as obtained from calibration).

515

516 **5 RESULTS**

517 ^{GA}SAKe was applied to shallow-landslide occurrences in the Sorrento Peninsula and to a medium-
518 size slope movement at San Fili, by considering the dates of activation and the daily rainfall series
519 mentioned in section §4.1 and §4.2, and adopting the values of parameters listed in Table 4.
520 Among the kernels obtained from calibration, several provided similar fitness values. Thus,
521 “average kernels” were computed for the considered case studies, by averaging the best 100 kernels.

522

523 **5.1 Application to shallow landslides in the Sorrento Peninsula**

524 In Table 5, the statistics related to the best 100 filter functions obtained from calibration (optimal
525 kernels) are summarized. From such values, a low variability of Φ , t_b and μ_0 can be appreciated;
526 instead, Δz_{cr} shows a greater range of values. The average kernel is shown in Figure 10: it is
527 characterized by fitness = 0.806, $\Delta z_{cr} = 0.00282$, and $t_b = 28$ days. From such kernel, antecedent
528 rainfall mostly affecting landslide instability range from 1 to 12 days, and subordinately from 25 to
529 26 days (negligible weights refer to rains occurred in the remaining period).
530 The mobility function related to the average kernel is shown in Fig. 11. In this case, 4 out of 10
531 dates of landslide activation are well captured by the model (being ranked at the first 7 positions of
532 the mobility function maxima); the remaining 6 dates do also correspond to relative maxima of the
533 function, but are ranked from the 43rd to the 151st position. When considering the remaining relative
534 maxima, several false positives can be recognized, mainly up to 1979.
535 During calibration, the best fitness ($\Phi = 0.807$) was first reached after 1749 iterations (at 6th
536 individual), with $\Delta z_{cr} = 0.00441$ and $t_b = 26$ days. The kernel corresponding to such individual looks
537 similar to the best one in terms of t_b , Δz_{cr} , and μ_0 (Fig. 12). The pattern of the best kernel is only
538 slightly dissimilar from the average one: significant weights can, in fact, be appreciated up to 14
539 days, and then between 20-22 and 25-26 days.
540 By applying the average kernel, a validation was performed against the remaining date of activation
541 (cf. Table 1, #11, multiple event occurred on 10 January 1997). Validation resulted fully satisfied,
542 as shown in Fig. 13: the value of the mobility function for the event #11 is well above the z_{cr}
543 threshold (49.01 vs. 18.05), and is ranked as the second highest value among the function maxima
544 (Fig. 13a). The same peak can also be appreciated as the maximum of the period $\pm t_b$ (Fig. 13b).
545 Accordingly, if adopting the average kernel, the event #11 of landslide activation could properly be
546 predicted by the model.

547 548 **5.2 Application to the Uncino landslide**

549 In Table 6, the statistics related to the family of optimal kernels are summarized. From such values,
550 a low variability of t_b and Δz_{cr} can be appreciated. The average kernel (Fig. 14) is characterized by
551 fitness = 1, $\Delta z_{cr} = 0.0644$, and $t_b = 66$ days. Based on such kernel, antecedent rains from 1 to 17
552 days, and from 27 to 45 days, mainly affect landslide instability. Relatively smaller weights pertain
553 to the rains occurred more than 53 days before the triggering; for periods older than 66 days, the
554 weights are negligible.
555 In Fig. 15, the mobility function related to the average kernel highlights that all the 5 dates of
556 activation are well captured by the model (they are ranked at the first 5 positions among the
557 function maxima). When considering the remaining relative maxima of the function, only 4 of them
558 evidence quasi-critical situations (between 1965 and 1966, and subordinately in 1970 and 1977).
559 During calibration, the best fitness ($\Phi = 1$) was first reached after 684 iterations (at 13th individual)
560 with $\Delta z_{cr} = 0.0595$. The best kernel (Fig. 16) was obtained at iteration 993, at 8th individual, with
561 $\Delta z_{cr} = 0.0631$. Its pattern results very similar to the average one, with a t_b of 66 days.
562 By applying the average kernel, a validation was performed against the last known date of
563 activation (cf. Table 2, #6, occurred on December 1980). Validation resulted fully satisfied, as
564 shown in Fig. 17: the value of the mobility function for the event #6, in fact, is well above the z_{cr}
565 threshold (17.49 vs. 16.87), and is ranked as the sixth highest value among the function maxima
566 (Fig. 17a). The same peak can be appreciated as the maximum of the period $\pm t_b$ (Fig. 17b).
567 Accordingly, if adopting the average kernel, the event #6 could properly be predicted by the model.

568
569
570
571
572
573
574
575
576
577
578
579
580
581
582
583
584
585
586
587
588
589
590
591
592
593
594
595
596
597
598
599
600
601
602
603
604
605
606
607
608
609
610
611

6 SELF-ADAPTIVE PROCEDURE AND SENSITIVITY ANALYSES

The capability of the model to react and self-adapt to input changes, such as new dates of landslide activation, was evaluated by a progressive, self-adaptive procedure of calibration and validation, using the information available for the Uncino case study. To simulate the adoption of $^{GA}SAKe$ in a landslide warning system, the model was iteratively calibrated by the first 2, 3, 4, and 5 dates of activation (L), and validated against the remaining 4, 3, 2, 1 dates, respectively. In each experiment, the GA-parameters listed in Table 4 were adopted. Finally, the model was merely calibrated by considering all the 6 dates of activation. The results of the self-adaptive procedure are listed in Table 7. The related kernels are shown in Fig. 18. As a result, a progressive increase in fitness and predictive ability (Δz_{cr}), together with the base time (ranging from 30 to 80 days), can be appreciated when employing a greater number of dates of activation.

Furthermore, aiming at evaluating the sensitivity of the model with respect to the GA parameters, a series of analyses was performed by considering again the Uncino case study. The experiments carried out are listed in Table 8. Each simulation stopped after 1500 iterations: GA-parameters were initialized by considering the “benchmark experiment” (cf. values in Table 4), except for the parameter that was in turn varied, as indicated in Table 8. The obtained maximum fitness (Φ_{max}), safety margin (Δz_{cr}), number (n_i) of iterations needed to first reach Φ_{max} , and base time (t_b) of the average kernel are shown in Fig. 19. If experiments with $\Phi_{max} = 1$ are only taken into account, the minimum and maximum numbers of GA-iterations needed to reach Φ_{max} (min_A, max_A), the minimum and maximum base times of the average kernel (min_t_b, max_t_b), and the minimum and maximum safety margins of the average kernel ($min_ \Delta z_{cr}, max_ \Delta z_{cr}$) are listed in Tables 9, 10 and 11, respectively.

7 DISCUSSION E CONCLUSIONS

In the present paper, the model $^{GA}SAKe$ is presented with examples of application to shallow-landslides in Sorrento Peninsula (Campania), and to the medium-size Uncino landslide at San Fili (Calabria). Furthermore, the capability of the model to simulate the occurrence of known landslide activations was evaluated by a progressive, self-adaptive procedure of calibration and validation against the Uncino case study. Finally, the sensitivity of the model with respect to the GA parameters was analysed by a series of experiments, performed again by considering the latter landslide.

As concerns the Sorrento Peninsula case study, the maximum fitness obtained during calibration is smaller than unity. For the best 100 kernels, Φ_{max} , Δz_{cr} and t_b vary in a small range (ca. 0.1%, 4.8%, and 13%, respectively). Furthermore, as mentioned above, for specific types of application (e.g., civil protection), the observed small values of Δz_{cr} would imply short warning times. Consequently, a suitable kernel should be rather selected by privileging the shortest t_b or the smallest μ_0 . From Fig. 12, it can be noticed that the greatest weights for the first 12-15 days are obtained by selecting the kernel characterized by the smallest μ_0 , thus allowing for the most timely advice if used within an early-warning system. In the average kernel, the greatest weight can be attributable to the first 12 days, with a maximum base time of about 4 weeks, reflecting the general shape of the curves in Fig. 7, and in good agreement with the shallow type of slope instability considered. Furthermore, the validation of the average kernel is satisfactory, as the validation date (#11 in Table 1) corresponds to the second highest peak of the mobility function. In addition, no missing alarms and only four

612 false alarms in about 5 years are to be found (i.e., in the period from the last date used for
 613 calibration to the one for validation). The peaks of the mobility function corresponding to the
 614 activation dates can roughly be grouped in two sets, characterized by distinct values: a first set, with
 615 $z(t) > 40$, generally includes the ancientmost plus the validation dates (#1, #2, #4, #5, #6, and #11); a
 616 second set (#3, #7, #8, #9, and #10), with $18 < z(t) < 25$. False alarms result more frequent and higher
 617 in the first period (from 1963 to 1980), presumably due to a lack of information on landslide
 618 activations.

619 Regarding the Uncino case study, the maximum fitness in calibration reaches unity. With respect to
 620 the Sorrento Peninsula case study, Δz_{cr} and t_b of the best 100 kernels vary in a greater range (ca.
 621 25%, and 30.5%, respectively), with Δz_{cr} one order of magnitude greater. In this case, the kernel
 622 would in fact allow for a safety margin of ca. 5%. In the average kernel, three main periods can be
 623 recognized with heavier weights, attributable to *i*) the first 17 days, *ii*) 27-45 days, and *iii*) 54-58
 624 days. The base time ranges from about 8 to 12 weeks, in good agreement with the medium-size type
 625 of the considered slope instability. Furthermore, the validation of the average kernel performed
 626 successfully: in fact, the validation date (#6 in Table 2) corresponds to the third highest peak of the
 627 mobility function; even in this case, neither missing alarms nor false alarms in about 2 years (from
 628 the last date calibration date to the validation one) are to be found. The peaks of the mobility
 629 function corresponding to the activation dates are characterized by $z(t) > 18$.

630 In the self-adaptive procedure applied to the Uncino case study, values for $L=6$ merely refer to
 631 calibration, whilst the ones for $2 \leq L \leq 5$ concern validation. With regard to Table 7 and Fig. 20, it can
 632 be noticed that:

- 633 • for $2 \leq L \leq 5$, t_b increases 2.7 times with L , and then remains constant for $L \geq 5$;
- 634 • from $L=2$ to $L=4$, z_{j-min} and z_{cr} slightly decrease, and then abruptly increase for $L \geq 5$;
- 635 • for $L \geq 4$, Δz_{cr} monotonically increases 72 times with L (being almost constant in the 2-4
 636 transition);
- 637 • Φ_v monotonically increases 1.7 times with L .

638 As a whole, a satisfying performance is obtained starting from 3 dates (i.e., correct predictions in
 639 more than 3 out of 4 times). For $L=5$, only one false alarm is observed. Finally, the calibration
 640 performed by considering all the 6 dates of activation provided fully satisfying results. Accordingly,
 641 the results of the progressive procedure underlined how *GASAKE* can easily self-adapt to external
 642 changes by optimizing its performances, providing increasing fitness values.

643 The average kernels obtained by considering from 2 to 6 dates of landslide activation show
 644 increasing base times, with significant weights for the ancientmost rains of the temporal range (Fig.
 645 18). Such result is in good accordance with the extent of the slope movement and, therefore, with
 646 the expected prolonged travel times of the groundwater affecting landslide activation.

647 In the sensitivity analyses, again performed by considering the Uncino landslide, $\Phi_{max} = 1$ was
 648 obtained in 60% of the experiments (cf. Table 8). The results (cf. Fig. 19 and Tables 9, 10, and 11)
 649 permit to select the set of parameters that allow for faster GA performances. More in detail:

- 650 • a ratio between the number of elitist individuals and the whole population of $n_e/N=10/20$ or
 651 $8/15$ allow for the fastest GA performances ($min_A_i \sim 41\%$ of the reference value);
 652 nevertheless, for increasing both n_e and N , this effect seems to vanish (e.g., $n_e/N=12/25$);
- 653 • with respect to the benchmark experiment, the explored changes in p_c , p_m , p_{mh1} , p_{me} , and p_{mtb} do
 654 not substantially affect the GA performances with respect to min_A_i ;

- 655 • with respect to the benchmark experiment, the explored changes of parameters determine
656 variation of t_b from 66 to 219%;
- 657 • in case of civil protection applications, the combination of parameters with $p_{mhl}=55$ allows for
658 activating early-warning procedures with the greatest advance;
- 659 • concerning $max_ \Delta z_{cr}$, the best result (increase by 10 times) is obtained when reducing N to 15.

660 The calibration experiments discussed in this paper were performed on a standard PC platform
661 (CPU 3 GHz, RAM 4 GB, standalone system SQL and application process). For the study cases of
662 Sorrento Peninsula and Uncino landslide, 2.5 and 1.1 GA-iterations were respectively performed
663 per minute, reaching Φ_{max} in 11^h40^m and 10^h20^m. Depending on availability of High-Performance
664 Computing Clusters, the mentioned durations may strongly be reduced, thus allowing for prompt
665 Civil Protection applications, e.g. based on short-term weather forecasts. By the way, the time
666 needed to calibrate the model can profitably be shortened by properly initializing the kernel, based
667 on expected characteristics of the phenomena under consideration (e.g., the range of t_b strongly
668 depends on landslide size).

669 In this study, a 2-steps efficiency criterion was employed: the relative position of the peaks of the
670 mobility function with respect to the dates of landslide activation was first considered, and the
671 fitness computed. Based on the value of Δz_{cr} , the obtained solutions were further ranked. Average,
672 synthetic filter functions could then be computed by selecting the best 100 kernels for successive
673 validation purposes. Alternative metrics (cf., among the others, Krause et al., 2005) for the fitness
674 function are being tested. However, due to uncertainties concerning input data (i.e., rainfall and
675 dates of landslide activation), the adoption of sophisticated techniques does not sound very
676 promising. In addition, problems of over-fitting may depend on both data uncertainties and number
677 of parameters. Commonly, kernels characterized by a complex pattern (and then by many
678 parameters) are needed for simulating groundwater dynamics (Pinault et al., 2001). Nevertheless,
679 more complex kernels do not necessarily imply higher predictive uncertainties (Fienen et al., 2010;
680 Long, 2015). Still, the adopted discrete approach allows focusing only on the timing of the peaks of
681 the mobility function, thus somehow relieving the computational effort. Due to the cited
682 uncertainties in input data, a “temporal window” was in fact employed to help matching dates of
683 activation with the peaks of the mobility function. Further attempts of defining the fitness function
684 by different metrics, and the analysis of its effects on calibration and validation, are being
685 considered against another case study (San Benedetto Ullano, in Calabria, Southern Italy), whose
686 mobility phases have been recently monitored by the same authors (Iovine et al., 2010; Capparelli et
687 al., 2012).

688 As mentioned above, model calibration may be hampered by either quality or completeness of input
689 data. Commonly, missing dates of activation (mainly in remote periods or in isolated areas) and
690 unsuitability of the rain gauge network (e.g., due to excessive distance of gauges from the
691 landslides) negatively affect model results. Depending on availability of new dates of activation,
692 stemming from further mobilizations or improvement of historical investigations, the predictive
693 capability of the model can be increased through additional calibrations, hence providing new
694 families of optimal solutions, constituted by fewer, highly significant kernels.

695 The above considerations suggest an indirect link between the model – despite empirical in type –
696 and the physical characteristics of the slope movements (e.g., dimensions, permeability, initial
697 water content of the slope, length of subsurface water paths). In general, to select the kernel to be

698 applied, it is rather preferable to consider a set of optimal kernels or the average one, instead of a
699 single solution.

700 Further efforts are in progress to improve the model and its chances of practical application, mainly
701 concerning the implementation of different GA techniques of optimization (in addition to the elitist,
702 here employed), the parallelization of the model, and the adoption of a Genetic Programming
703 approach. Finally, through the analytical study of the optimal kernels, a mathematical formulation
704 of discrete filter functions is presently being attempted, aiming at synthesizing optimal and average
705 kernels for an easier comparison with the results of other models available in literature.

706

707 **8 CODE AVAILABILITY**

708 The release ^{GA}SAKe of the *Self Adaptive Kernel* model, discussed in this paper, has been developed
709 by scientists working at CNR-IRPI under Microsoft Windows, Visual Studio, and SQL Server
710 integrated development environment. It can be requested by the public to the corresponding author
711 of the paper, together with examples of input data and technical support (a user manual is not
712 available yet, but it should be released soon). The model is presently undergoing further refinements
713 and developments, mainly concerning types of GA-selection techniques, the post-processing of the
714 results in terms of continuous analytical functions, and the implementation of a library of case
715 studies. Authors are willing to cooperate with external users to further improving the model through
716 applications to case studies from different geo-environmental contexts.

717

718 **ACKNOWLEDGEMENTS**

719 For the rainfall series of the Calabrian rain gauges, we are grateful to: *Regione Calabria*, Ing.
720 Raffaele Niccoli, *Direttore del Centro Funzionale Multirischi dell'ARPACal*.

721 For the rainfall series of the Campanian rain gauges, we are grateful to: *Regione Campania*, Ing.
722 Generoso Schiavone, *Dirigente del Settore "Programmazione Interventi di Protezione Civile sul*
723 *Territorio"*, and Ing. Mauro Biafore, *Dirigente del Servizio 04, Responsabile CFD "Centro*
724 *funzionale per la previsione meteorologica e il monitoraggio meteo-idro-pluviometrico e delle*
725 *frane"*.

726 Finally, we thank the Editors and two anonymous Referees for their constructive comments and
727 insights that allowed us to considerably improve the manuscript.

728

729 **REFERENCES**

- 730 Aleotti, P.: A warning system for rainfall-induced shallow failures, *Eng. Geol.*, 73, 247–265, 2004.
- 731 Alfieri, L., Salamon, P., Pappenberger, F., Wetterhall, F., and Thielen, J.: Operational early warning
732 systems for water-related hazards in Europe, *Environ. Sci. Policy*, 21, 35–49, 2012.
- 733 Amodio-Morelli, L., Bonardi, G., Colonna, V., Dietrich, D., Giunta, G., Ippolito, F., Liguori, V.,
734 Lorenzoni, S., Paglionico, A., Perrone, V., Piccarreta, G., Russo, M., Scandone, P., Zanettin
735 Lorenzoni, E., and Zuppetta, A.: L'arco calabro-peloritano nell'orogene appenninico-
736 maghrebide, *Mem. Soc. Geol. Ital.*, 17, 1–60, 1976 (in Italian).
- 737 AMRA: Overview of intense rainfall on volcanic soils—regional and local scale, in: *SafeLand -*
738 *Living with landslide risk in Europe: Assessment, effects of global change, and risk*
739 *management strategies*, edited by: Crosta, G.B., Agliardi, F., Frattini, P., Sosio, R., 101–122.
740 2012.

741 Berti, M., Martina, M.L.V., Franceschini, S., Pignone, S., Simoni, A., and Pizziolo, M.:
742 Probabilistic rainfall thresholds for landslide occurrence using a Bayesian approach, *J.*
743 *Geophys. Res.*, 117, F04006, <http://dx.doi.org/10.1029/2012JF002367>, 2012.

744 Brand, E.W., Premchitt, J., and Phillipson, H.B.: Relationship between rainfall and landslides, in:
745 *Proceedings of the 4th International Symposium on Landslides, Toronto, vol. 1, BiTech*
746 *Publishers, Vancouver, Canada, 377–384, 1984.*

747 Brunetti, M.T., Peruccacci, S., Rossi, M., Luciani, S., Valigi, D. and Guzzetti, F.: Rainfall
748 thresholds for the possible occurrence of landslides in Italy, *Nat. Hazards Earth Syst. Sci.*, 10,
749 447–458, 2010.

750 Brunsdon, D.: Mudslides, in: *Slope Instability*, edited by Brunsdon, D., and Prior, D.B., John Wiley
751 & Sons, London, 363–418, 1984.

752 Caine, N.: The rainfall intensity-duration control of shallow landslides and debris flows,
753 *Geografiska Annal*, 62A, 23–27, 1980.

754 Calcaterra, D., and Santo, A.: The January 10, 1997 Pozzano landslide, Sorrento Peninsula, Italy,
755 *Eng. Geol.*, 75, 181–200, 2004.

756 Campbell, R.H.: Debris flow originating from soil slip during rainstorm in southern California, *Q. J.*
757 *Eng. Geol.*, 7, 377–384, 1975.

758 Cannon, S.H., and Ellen, S.D.: Rainfall conditions for abundant debris avalanches, San Francisco
759 Bay region, California, *California Geology*, 38 (12), 267–272, 1985.

760 Capparelli, G., and Versace, P.: FLAIR and SUSHI: two mathematical models for early warning of
761 landslides induced by rainfall, *Landslides*, 8, 67–79, 2011.

762 Capparelli, G., Iaquina, P., Iovine, G., Terranova, O.G., and Versace P.: Modelling the rainfall-
763 induced mobilization of a large slope movement in northern Calabria, *Nat. Hazards*, 61(1),
764 247–256, 2012.

765 Carter, J.: The notion of Threshold: an investigation into conceptual accompaniment in Aristotle
766 and Hegel, *Conserveries mémorielles*, 7, available at: <http://cm.revues.org/431>, last access: 10
767 December 2014, 2010.

768 Cascini, L., and Versace, P.: Eventi pluviometrici e movimenti franosi, in: *Atti del XVI Convegno*
769 *Nazionale di Geotecnica, Bologna, Italy, 14-16 may 1986, 171–184, 1986 (in Italian).*

770 Cascini, L., and Versace, P.: Relationship between rainfall and landslide in a gneissic cover, in:
771 *Proceedings of the 5th International Symposium on Landslides, Lausanne, Switzerland, 565–*
772 *570, 1988.*

773 Cascini, L., Sorbino, G., Cuomo, S., Ferlisi, S.: Seasonal effects of rainfall on the shallow
774 pyroclastic deposits of the Campania region (southern Italy), *Landslides*, 11, 779–792, 2014.

775 CASMEZ: Carta Geologica della Calabria, F.229IINE “Montalto Uffugo” (in scale 1:25000),
776 Poligrafica & CarteValori, Ercolano, Napoli, Italy, 1967 (in Italian).

777 Cauvin, S., Cordier, M.-O., Dousson, C., Laborie, P., Lévy, F., Montmain, J., Porcheron, M.,
778 Servet, I., and Travé-Massuyès, L.: Monitoring and alarm interpretation in industrial
779 environments, *AI Commun.*, 11 (3–4), 139–173, 1998.

780 Chow, V.T., Maidment, D.R., and Mays, L.W.: *Applied Hydrology*, Mc Graw Hill, New York,
781 USA, 572 pp., 1988.

782 Corominas, J.: Landslides and climate, Keynote lecture, in: *Proceedings of the 8th International*
783 *Symposium on Landslides, vol. 4, Cardiff, United Kingdom, 26-30 June 2000, 1-33, 2000.*

784 Crosta, G.B.: Regionalization of rainfall thresholds: an aid to landslide hazard evaluation, *Environ.*
785 *Geol.*, 35 (2-3), 131–145, 1998.

786 Crosta, G.B., Dal Negro, P, and Frattini, P.: Soil slips and debris flows on terraced slopes, *Nat.*
787 *Hazards Earth Syst. Sci.*, 3, 31–42, 2003.

788 Crozier, M.J.: The climate-landslide couple: a southern hemisphere perspective, in: *Rapid mass*
789 *movement as a source of climatic evidence for the Holocene*, edited by: Matthews, J.A.,
790 Brunsdon, D., Frenzel, B., Gläser, B., and Weiß, M.M., Gustav Fischer, Stuttgart, 333–354,
791 1997.

792 Cuomo, S. and Della Sala, M.: Rainfall-induced infiltration, runoff and failure in steep unsaturated
793 shallow soil deposits, *Eng. Geol.*, 162, 118–127, 2013.

794 D’Ambrosio, D., Spataro, W., and Iovine, G.: Parallel genetic algorithms for optimising cellular
795 automata models of natural complex phenomena: an application to debris-flows, *Computer and*
796 *Geosciences*, 32, 861–875, 2006.

797 De Jong, K.A.: *An analysis of the behavior of a class of genetic adaptive systems*, Ph.D.
798 dissertation, Department of Computer and Communication Sciences, University of Michigan,
799 Ann Arbor, USA, 1975.

800 Del Prete, M., Guadagno, F.M., and Hawkins, A.B.: Preliminary report on the landslides of 5 May
801 1998, Campania, southern Italy, *Bull. Eng. Geol. Env.*, 57, 113–129, 1998.

802 Di Crescenzo, G., and Santo, A.: Analisi morfologica delle frane da scorrimento-colata rapida in
803 depositi piroclastici della Penisola Sorrentina (Campania), *Geografia Fisica e Dinamica*
804 *Quaternaria*, 22, 57–72, 1999 (in Italian).

805 Di Crescenzo, G., and Santo, A.: Debris slides-rapid earth flows in the carbonate massifs of the
806 Campania region (Southern Italy): morphological and morphometric data for evaluating
807 triggering susceptibility, *Geomorphology*, 66, 255–276, 2005.

808 Dikau, R., and Schrott, L.: The temporal stability and activity of landslides in Europe with respect
809 to climatic change (TESLEC): main objectives and results, *Geomorphology*, 30 (1–2), 1–12.
810 1999.

811 Ducci, D., and Tranfaglia, G.: L’impatto dei cambiamenti climatici sulle risorse idriche sotterranee
812 in Campania, *Geologi. Boll. Ordine Geologi della Campania*, 1–4, 13–21, 2005 (in Italian).

813 Ellen, S.D.: Description and mechanics of soil slip/debris flows in the storm, in: *Landslides, floods,*
814 *and marine effects of the storm of January 3-5, 1982, in the San Francisco Bay region,*
815 *California*, edited by Ellen, S.D., and Wieczorek, G.F., U.S. Geol. Surv. Prof. Pap., 1434, 63–
816 112, 1988.

817 Fienen, M.N., Doherty, J.E., Hunt, R.J., and Reeves, H.W.: Using prediction uncertainty analysis to
818 design hydrologic monitoring networks: example applications from the Great Lakes water
819 availability pilot project, US Geol. Surv., Reston Virginia, Scientific Investigations Report
820 2010-5159, 44 pp., 2010.

821 Fiorillo, F., and Wilson, R.: Rainfall induced debris flows in pyroclastic deposits, Campania
822 (southern Italy), *Eng. Geol.*, 75, 263–289, 2004.

823 Gariano, S.L., Brunetti, M.T., Iovine, G., Melillo, M., Peruccacci, S., Terranova, O., Vennari, C.,
824 and Guzzetti, F.: Calibration and validation of rainfall thresholds for shallow landslide
825 forecasting in Sicily, southern Italy, *Geomorphology*, 228, 653–665, 2015.

826 Goldberg, D.E.. *Genetic Algorithms in Search, Optimization and Machine Learning*, Addison-
827 Wesley, Boston, USA, 1989.

828 Gullà, G., Aceto, L., Antronico, L., Cilento, M., Niceforo, D., Perna, E., and Terranova, O.: Failure
829 and post failure conditions of a landslide involving weathered and degraded rocks, in

830 Proceedings of the IX International Symposium on Landslide, Rio de Janeiro, Brazil, 28 June -
831 2 July 2004, 1241–1245, 2004.

832 Guzzetti, F.: Landslide fatalities and evaluation of landslide risk in Italy, *Eng. Geol.*, 58, 89–107,
833 2000.

834 Guzzetti, F., Peruccacci, S., Rossi, M., and Stark, C.P.: Rainfall thresholds for the initiation of
835 landslides in central and southern Europe, *Meteorol. Atmos. Phys.*, 98, 239–267, 2007.

836 Guzzetti, F., Peruccacci, S., Rossi, M., and Stark, C.P.: The rainfall intensity-duration control of
837 shallow landslides and debris flow: an update, *Landslides*, 5, 3–17, 2008.

838 Hinton, G.E., and Nowlan, S.J.: How learning can guide evolution, *Complex Systems*, 1, 495–502,
839 1987.

840 Holland, J.H.: *Adaptation in Natural and Artificial Systems*. University of Michigan Press, Ann
841 Arbor, USA, 1975.

842 Hutchinson, J.N.: Deep-seated mass movements on slopes, *Mem. Soc. Geol. It.*, 50, 147–164, 1995.

843 Iovine, G., D’Ambrosio, D., and Di Gregorio, S.: Applying genetic algorithms for calibrating a
844 hexagonal cellular automata model for the simulation of debris flows characterised by strong
845 inertial effects, *Geomorphology*, 66, 287–303, 2005.

846 Iovine, G., Iaquina, P., and Terranova, O.: Emergency management of landslide risk during
847 Autumn-Winter 2008/2009 in Calabria (Italy). The example of San Benedetto Ullano, in:
848 Proceedings of the 18th World IMACS Congress and MODSIM09 International Congress on
849 Modelling and Simulation, Modelling and Simulation Society of Australia and New Zealand
850 and International Association for Mathematics and Computers in Simulation, July 2009, 2686–
851 2693, 2009.

852 Iovine, G., Lollino, P., Gariano, S.L., and Terranova, O.G.: Coupling limit equilibrium analyses and
853 real-time monitoring to refine a landslide surveillance system in Calabria (southern Italy), *Nat.*
854 *Hazards Earth Syst. Sci.*, 10, 2341–2354, 2010.

855 Jakob, M., and Weatherly, H.: A hydroclimatic threshold for landslide initiation on the North Shore
856 Mountains of Vancouver, British Columbia, *Geomorphology*, 54, 3–4, 137–156, 2003.

857 Keefer, D.K., Wilson, R.C., Mark, R.K., Brabb, E.E., Brown III W.M., Ellen S.D., Harp E.L.,
858 Wieczorek G.F., Alger C.S., and Zatkan, R.S.: Real-Time Landslide Warning During Heavy
859 Rainfall, *Science*, 238 (4829), 921–925, 1987.

860 Köppen, W.: *Climatologia, con un estudio de los climas de la tierra*, Fondo de Cultura Economica,
861 Mexico, 479 pp., 1948.

862 Krause, P., Boyle D.P., and Båse, F.: Comparison of different efficiency criteria for hydrological
863 model assessment, *Adv. Geosciences*, 5, 89–97, 2005

864 Lanzafame, G., and Mercuri, T.: Interruzioni ferroviarie in Calabria conseguenti a fenomeni naturali
865 (1950–1973), *Geodata*, 3, Cosenza, Italy, 46 pp., 1975 (in Italian).

866 Long, A.J.: RRAWFLOW: Rainfall-Response Aquifer and Watershed Flow Model (v1.15), *Geosci.*
867 *Model Dev.*, 8, 865–880, 2015.

868 Marques R., Zêzere J., Trigo R., Gaspar J., and Trigo, I.: Rainfall patterns and critical values
869 associated with landslides in Povoação County (São Miguel Island, Azores): relationships with
870 the North Atlantic Oscillation, *Hydrol. Process.*, 22(4), 478–494, 2008.

871 Mele, R., and Del Prete, S.: Lo studio della franosità storica come utile strumento per la
872 valutazione della pericolosità da frane. Un esempio nell’area di Gragnano (Campania), *Boll.*
873 *Soc. Geol. Ital.*, 118, 91–111, 1999 (in Italian).

874 Mitchell, M.: An Introduction to Genetic Algorithms, MIT Press, Cambridge, United Kingdom,
875 1996.

876 Monaco, C., and Tortorici, L.: Active faulting in the Calabrian arc and eastern Sicily, *J. Geodyn.*,
877 29, 407–424, 2000.

878 Montgomery, D.R., and Dietrich, W.E.: A physically-based model for the topographic control on
879 shallow landsliding, *Water Resour. Res.*, 30, 1153–1171, 1994.

880 Nolfi, S., and Marocco, D.: Evolving robots able to integrate sensory-motor information over time,
881 *Theor Biosci*, 120, 287–310, 2001.

882 Peres, D.J., and Cancelliere, A.: Derivation and evaluation of landslide-triggering thresholds by a
883 Monte Carlo approach, *Hydrol. Earth Syst. Sci.*, 18, 4913–4931, 2014.

884 Petley, D.N.: The global occurrence of fatal landslides in 2007, in: International Conference on
885 Management of Landslide Hazard in the Asia-Pacific Region, Tokyo, Japan, 590–600, 2008.

886 Pinault, J.-L., Plagnes, V., and Aquilina, L.: Inverse modeling of the hydrological and the
887 hydrochemical behavior of hydrosystems: Characterization of karst system functioning, *Water*
888 *Resour. Res.*, 37(8), 2191–2204, 2001.

889 Pisani, G., Castelli, M., and Scavia, C.: Hydrogeological model and hydraulic behaviour of a large
890 landslide in the Italian Western Alps, *Nat. Hazards Earth Syst. Sci.*, 10, 2391–2406, 2010.

891 Poon, P.W., and Parks, G.T.: Optimizing PWR reload core design, *Parallel Solving from Nature*, 2,
892 371–380, 1992.

893 Pradhan, B., and Buchroithner, M.: *Terrigenous Mass Movements: Detection, Modelling, Early*
894 *Warning and Mitigation Using Geoinformation Technology*, Springer, 400 pp., 2012.

895 Rossi, F., and Villani, P. (eds.): *Valutazione delle piene in Campania*, CNR-GNDCI publications,
896 *Grafica Metellioana &C.*, Cava de' Tirreni, Italy, 310 pp., 1994.

897 Salvati, P., Bianchi, C., Rossi, M., and Guzzetti, F.: Societal landslide and flood risk in Italy. *Nat.*
898 *Hazards Earth Syst. Sci.*, 10, 465–483, 2010.

899 Sengupta, A., Gupta, S., and Anbarasu, K.: Rainfall thresholds for the initiation of landslide at
900 Lanta Khola in north Sikkim, India, *Nat. Hazards*, 52, 31–42, 2010.

901 Servizio Geologico, Sismico dei Suoli: *I numeri delle frane*, Regione Emilia-Romagna Publisher,
902 Bologna, 94 pp., 1999 (in Italian).

903 Servizio Idrografico: *Annali Idrologici*, Parte I, Compartimento di Napoli, Istituto poligrafico e
904 Zecca dello Stato, Rome, Italy, 1948-1999.

905 Sirangelo, B., and Versace, P.: A real time forecasting for landslides triggered by rainfall,
906 *Meccanica*, 31, 1–13, 1996.

907 Sorriso-Valvo, G.M., Agnesi, V., Gulla, G., Merenda, L., Antronico, L., Di Maggio, C., Filice, E.,
908 Petrucci, O., and Tansi, C.: Temporal and spatial occurrence of landsliding and correlation with
909 precipitation time series in Montalto Uffugo (Calabria) and Imera (Sicilia) areas, in: *Temporal*
910 *occurrence and forecasting of landslides in the European Community. Final Report, II*,
911 *European Community, Programme EPOCH, Contract 90 0025*, edited by Casale, R., Fantechi,
912 R., Flageollet, J.C., 825–869, 1994.

913 Sorriso-Valvo, G.M., Antronico, L., Catalano, E., Gullà, G., Tansi, C., Dramis, F., Ferrucci, F., and
914 Fantucci, R.: *Final Report (June 1996)*, CNR-IRPI, in: *The temporal stability and activity of*
915 *landslides in Europe with respect to climatic change (TESLEC), Final Report, Part II*, edited
916 by: Dikau, R., Schrot, L., Dehn, M., Hennrich, K., and Rasemann, S., 87–152. 1996.

917 Terlien, M.T.J.: The determination of statistical and deterministic hydrological landslide-triggering
918 thresholds, *Environ. Geol.*, 35 (2-3), 125–130, 1998.

919 Terranova, O.: Caratteristiche degli eventi pluviometrici a scala giornaliera in Calabria, in: XXIX
920 Convegno di Idraulica e Costruzioni Idrauliche, Trento, Italy, 7-10 september 2004, 343-350,
921 2004 (in Italian).

922 Terranova, O., Antronico, L., and Gullà, G.: Pluviometrical events and slope stability on weathered
923 and degraded rocks (Acri, Calabria, Italy), in Proceedings of the IX International Symposium
924 on Landslide, Rio de Janeiro, Brazil, 28 June - 2 July 2004, 335-342, 2004.

925 Terranova, O., Iaquina, P., Gariano, S.L., Greco, R., and Iovine, G.: *CM SAKe*: A hydrological
926 model to forecasting landslide activations, in: Landslide Science and Practice, vol. 3, edited by:
927 Margottini, C., Canuti, P., and Sassa K., Springer, 73-79, 2013.

928 Terzaghi, K.: Stability of steep slopes on hard unweathered rock, *Geotechnique*, 12 (4), 251-270,
929 1962.

930 Trigila, A.: Rapporto sulle frane in Italia. Il Progetto IFFI. Metodologia, risultati e rapporti
931 regionali, APAT, Roma, Italy, 681 pp., 2007 (in Italian).

932 Trigo, R.M., Zêzere, J.L., Rodrigues, M.L., and Trigo, I.F.: The influence of the North Atlantic
933 Oscillation on rainfall triggering of Landslides near Lisbon, *Nat. Hazards*, 36 (3), 331-354,
934 2005.

935 UNDR0: Mitigating Natural Disasters. Phenomena, Effects and Options, United Nations, New
936 York, USA, 164 pp., 1991.

937 Van Asch, Th.V.J., Buma, J., and Van Beek, L.P.H.: A view on some hydrological triggering
938 systems in landslides, *Geomorphology*, 30 (1-2), 25-32, 1999.

939 Vennari, C., Gariano, S.L., Antronico, L., Brunetti, M.T., Iovine, G., Peruccacci, S., Terranova, O.,
940 and Guzzetti, F.: Rainfall thresholds for shallow landslide occurrence in Calabria, southern
941 Italy, *Nat. Hazards Earth Syst. Sci.*, 14, 317-330, 2014.

942 White, I.D., Mottershead, D.N., and Harrison, J.J.: *Environmental Systems*, 2nd Edition, Chapman
943 & Hall, London, United Kingdom, 616 pp., 1996.

944 Wieczorek, G.F.: Effect of rainfall intensity and duration on debris flows in central Santa Cruz
945 Mountains, California, in: *Debris Flows/Avalanches: Processes, Recognition and Mitigation*,
946 edited by: Costa, J.E., and Wieczorek GF, Geological Society of America, *Reviews in*
947 *Engineering Geology* 7, 93-104. 1987

948 Wieczorek, G.F., and Glade, T.: Climatic factors influencing occurrence of debris flows, in: *Debris*
949 *flow hazards and related phenomena*, edited by: Jakob, M. and Hungr, O., Berlin Heidelberg,
950 Springer, 325-362, 2005.

951 Wilson, R.C., and Wieczorek, G.F.: Rainfall thresholds for the initiation of debris flow at La
952 Honda, California, *Environ. Eng. Geosci.*, 1, 11-27, 1995.

953 Zêzere, J.L., and Rodrigues, M.L.: Rainfall thresholds for landsliding in Lisbon area (Portugal), in
954 *Landslides*, edited by: Rybar, J, Stemberk, J, and Wagner, P., A.A. Balkema, Lisse, The
955 Netherlands, 333-338, 2002.

957 **Table 1.** Dates of activation of the shallow landslides in the Sorrento Peninsula. Key: date = day of occurrence; type =
958 widespread (multiple) or few (single) activation; site = municipality including the affected location; period employed =
959 dates used for calibration (except for #11); rank = relative position of the corresponding maximum of the mobility
960 function obtained by calibration. An asterisk marks the date employed for validation. In Italics, the activation date (#0)
961 excluded due to hydrological constraints.
962

#	Date	type	site	reference	period employed	rank
1	17 February 1963	multiple; single	Gragnano, Pimonte; Castellammare	Del Prete et al. 1998	17 Feb 1963	17 Feb 1963 (1)
2	23 November 1966	single	Vico Equense (Scrajo), Arola, Ticciano	Del Prete et al. 1998	23 Nov 1966	24 Nov 1966 (4)
0	<i>14 April 1967</i>	<i>single</i>	<i>Castellammare (Pozzano)</i>	<i>Del Prete et al. 1998; AMRA, 2012</i>	-	-
3	15 March 1969; 24 March 1969	multiple; multiple	Cava de' Tirreni, Agerola, Scrajo Seiano	Del Prete et al. 1998; AMRA, 2012	15-24 Mar 1969	25 Mar 1969 (65)
4	02 January 1971	single	Gragnano	Del Prete et al. 1998	02 Jan 1971	3 Jan 1971 (3)
5	21 January 1971	single	Gragnano	Del Prete et al. 1998	21 Jan 1971	21 Jan 1971 (7)
6	04 November 1980	single	Vico Equense (Scrajo)	Del Prete et al. 1998	04 Nov 1980	6 Nov 1980 (94)
7	14 November 1982	single	Pozzano	Del Prete et al. 1998	14 Nov 1982	15 Nov 1982 (151)
8	22 February 1986	multiple	Palma Campania, Castellammare, Vico Equense	Del Prete et al. 1998	22 Feb 1986	24 Feb 1986 (120)
9	23 February 1987	single	Gragnano, Castellammare	Del Prete et al. 1998; AMRA, 2012	23 Feb 1987	23 Feb 1987 (73)
10	23 November 1991	single	Pozzano	Del Prete et al. 1998	23 Nov 1991	24 Nov 1991 (43)
11	10 January 1997	multiple	Pozzano; Castellammare, Nocera, Pagani, Amalfitana Coast	Del Prete et al. 1998 AMRA, 2012	10 Jan 1997	*

963

964

965 **Table 2.** Dates of activation of the Uncino landslide. Periods (instead of singular dates) were considered in case of
 966 uncertain timing of activation. Key = #: Identification number of the date (in bold, used for calibration); dates/periods
 967 derived from literature; dates/periods employed for calibration or validation; references: sources of information on
 968 activation dates; rank: relative position and dates of the maxima of the mobility function during calibration. An asterisk
 969 marks the activation employed for validation. In *Italics*, the activation date (#0) excluded due to hydrological
 970 constraints.
 971

#	date	reference	period	rank
1	16, 21 January 1960	Sorriso-Valvo et al., 1996	16-21 Jan 1960	18 Jan 1960 (5)
2	Winter 1963	Sorriso-Valvo et al., 1994	01 Nov 1962 – 14 Apr 1963	29 Mar 1963 (1)
3	15 April 1964 (h 22:00)	Sorriso-Valvo et al., 1994	15 Apr 1964	14 Apr 1964 (3)
4	14 December 1966	Lanzafame and Mercuri, 1975	14 Dec 1966	16 Dec 1966 (2)
5	10-14, 21 February 1979	Sorriso-Valvo et al., 1994	10-21 Feb 1979	15 Feb 1979 (4)
6	December 1980	Sorriso-Valvo et al., 1994	01-31 Dec 1980	*
<i>0</i>	<i>23 November 1988</i>	<i>Sorriso-Valvo et al., 1996</i>	-	-

972
 973

974 **Table 3.** Average monthly rainfall and number of rainy days at the Montalto Uffugo rain gauge (468 m a.s.l.).
975

	Sep	Oct	Nov	Dec	Jan	Feb	Mar	Apr	May	Jun	Jul	Aug	year
rainfall (mm)	70.4	125.1	187.9	220.8	198.1	160.3	132.8	98.9	64.6	27.8	18.3	28.6	1333.6
rainy days	6.9	10.6	12.8	14.3	14.3	12.5	12.6	10.7	8.26	4.7	2.62	3.84	114.0

976

977

978 **Table 4.** Values of the parameters of GA^{SAKe} adopted in the calibration procedure (benchmark experiment).

979

symbol	parameter	value
N	individuals of each GA population	20
t_b	base time (Uncino landslide)	30 ÷ 180 days
	base time (shallow landslides in the Sorrento Peninsula)	2 ÷ 30 days
p_{mh1}	percentages of the maximum height of the kernel, used to defining the range in which dh is randomly obtained	50%, 150%
p_{mh2}		
p_c	probability of crossover	75%
p_m	probability of mutation	25%
p_{me}	number of mutated elements of the kernel, expressed as a percentage of t_b	25%
p_{mib}	factor defining the range in which dt_b is selected	0.2 ÷ 5
A	number of GA-iterations (Uncino landslide case study)	5000
	number of GA-iterations (Sorrento Peninsula case study)	3000
n_e	number of "elitist" individuals	8

980

981

982 **Table 5.** Sorrento Peninsula case study. Statistics for the best 100 kernels.

983

	Φ	Δz_{cr}	t_b	μ_0
min	0.806	3.82E-05	26.0	9.460
average	0.806	0.00418	30.4	9.567
max	0.807	0.00801	31.0	10.448
median	0.806	0.00499	31.0	9.567
mode	0.806	0.00499	31.0	9.567
dev. st.	7.65E-05	0.00183	0.862	0.146

984

985

986 **Table 6.** Uncino landslide case study. Statistics for the best 100 kernels.

	Δz_{cr}	t_b
min	0.0524	57.0
average	0.0581	69.5
max	0.0692	82.0
median	0.0581	69.0
mode	0.0558	69.0
dev. st.	0.00373	3.12

987

988

989 **Table 7.** Uncino landslide case study. Results of progressive calibration. Key: L , t_b , z_{j-min} , z_{cr} , Δz_{cr}): model parameters
 990 concerning calibration (for explanation, cf. text); Φ_v) fitness obtained by validating the “average kernel”, obtained in
 991 calibration, against the 6 dates of activation. In *Italics*, results obtained when calibrating the model by using all the 6
 992 available dates (no validation performed).

L	t_b	z_{j-min}	z_{cr}	Δz_{cr}	Φ_v
2	30	13.93	13.89	0.0029	0.59
3	54	11.05	11.04	0.0009	0.78
4	55	10.21	10.20	0.0010	0.87
5	80	16.44	16.34	0.0061	0.95
<i>6</i>	<i>80</i>	<i>18.63</i>	<i>17.43</i>	0.0644	<i>1.00</i>

994

995

996 **Table 8.** Uncino landslide case study. Values of the parameters adopted in the sensitivity analyses. In bold, the
 997 experiments with $\Phi_{max} = 1$. Boxes evidence the worst experiment (in Italics), and the best one (underlined).
 998

<i>symbol</i>	<i>values</i>				
	6	7	^{a)} 8	9	<u>10</u>
n_e	6	7	^{a)} 8	9	<u>10</u>
p_c	60%	67.5%	^{a)} 75%	<u>82.5%</u>	90%
p_m	20%	22.5%	^{a)} 25%	27.5%	30%
p_{mh1}	60%	55%	^{a)} 50%	45%	40%
p_{mh2}	140%	145%	^{a)} 150%	155%	160%
p_{me}	20%	22.5%	^{a)} 25%	27.5%	30%
p_{mtb}	0.25 ÷ 4	0.22 ÷ 4.5	^{a)} 0.2 ÷ 5	0.18 ÷ 5.5	0.17 ÷ 6
N, n_e		25, 8	^{a)} 20, 8	15, 8	
N, n_e		25, 12	25, 10	25, 8	

^{a)} Reference values (i.e., those of the benchmark experiment - cf. Table 4)

999

1000

1001 **Table 9.** Minimum (min_{A_i}) and maximum (max_{A_i}) numbers of GA iterations needed to reach Φ_{max} (only experiments
1002 with $\Phi_{max} = 1$ are considered). In the first column, the letters refer to Fig. 19. In bold, the best and worst experiments.
1003 An asterisk marks the experiment e , in which Φ_{max} was reached only for $p_c=75$. In Italics, the combinations of
1004 parameters of the benchmark experiment (cf. Table 4).
1005

\S	N	<i>parameter</i>	min_{A_i}	max_{A_i}
<i>a</i>	20	$n_e=8$		<i>684</i>
a	20	$n_e=10$	279	
c	25	$n_e=8$	469	
c	25	$n_e=12$		1477
<i>e</i>	20	$p_c=75$	<i>684*</i>	
<i>g</i>	20	$p_m=25$	<i>684</i>	
g	20	$p_m=27.5$		1086
<i>i</i>	20	$p_{mhI}=50$	<i>684</i>	
i	20	$p_{mhI}=55$		836
<i>k</i>	20	$p_{me}=25$	<i>684</i>	
k	20	$p_{me}=30$		996
<i>m</i>	20	$p_{mb}=5$	<i>684</i>	
m	20	$p_{mb}=5.5$		1052
<i>o</i>	15	$n_e=8$	405	

1006

1007

1008 **Table 10.** Minimum (min_t_b) and maximum (max_t_b) base time of the average kernel (only experiments with $\Phi_{max} = 1$
1009 are considered). In the first column, the letters refer to Fig. 19. In bold, the best and worst experiments. An asterisk
1010 marks the experiment e , in which Φ_{max} was reached only for $p_c=75$. In Italics, the combinations of parameters of the
1011 benchmark experiment (cf. Table 4).
1012

\S	N	<i>parameter</i>	min_t_b	max_t_b
<i>a</i>	20	$n_c=8$	<i>66,59</i>	
a	20	$n_c=10$		144,85
c	25	$n_c=8$		132,00
c	25	$n_c=12$	56,17	
<i>e</i>	20	$p_c=75$	<i>66,59*</i>	
<i>g</i>	20	$p_m=25$	<i>66,59</i>	
g	20	$p_m=27.5$		139,20
<i>i</i>	20	$p_{mh}=50$		<i>66,59</i>
i	20	$p_{mh}=55$	44,00	
<i>k</i>	20	$p_{me}=25$	<i>66,59</i>	
k	20	$p_{me}=30$		146,93
<i>m</i>	20	$p_{mb}=5$	<i>66,59</i>	
m	20	$p_{mb}=4$		136,06
o	15	$n_c=8$		145,79

1013

1014

1015 **Table 11.** Minimum ($min_ \Delta z_{cr}$) and maximum ($max_ \Delta z_{cr}$) safety margin of the average kernel (only experiments with
1016 $\Phi_{max} = 1$ are considered). In the first column, the letters refer to Fig. 19. In bold, the best and worst experiments. An
1017 asterisk marks the experiment e , in which Φ_{max} was reached only for $p_e=75$. In Italics, the combinations of parameters of
1018 the benchmark experiment (cf. Table 4).
1019

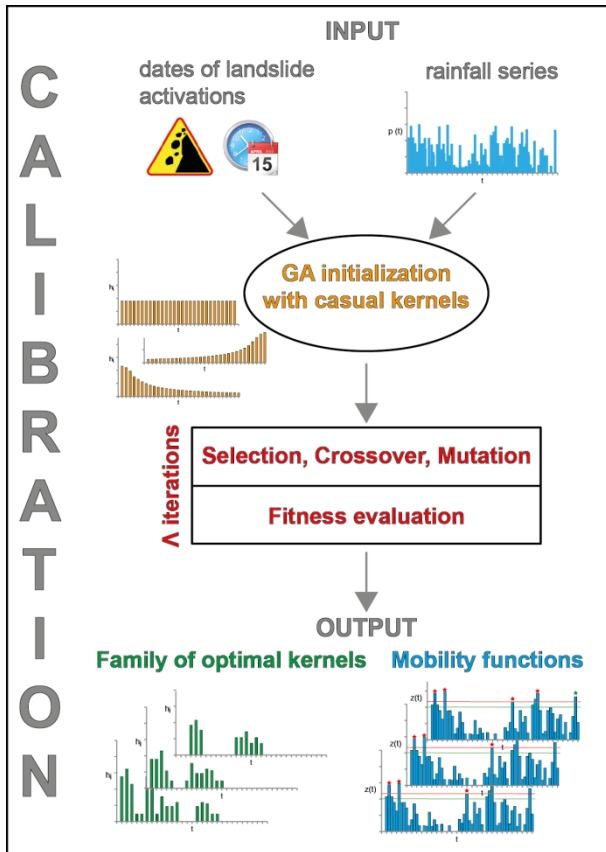
\S	N	<i>parameter</i>	$min_ \Delta z_{cr}$	$max_ \Delta z_{cr}$
a	20	$n_e=7$		0.007
a	20	$n_e=9$	0.002	
c	25	$n_e=8$		0.014
c	25	$n_e=12$	0.002	
<i>e</i>	20	$p_c=75$	<i>0.005*</i>	
g	20	$p_m=22.5$		0.006
g	20	$p_m=27.5$	0.001	
<i>i</i>	20	$p_{mhl}=50$		<i>0.005</i>
i	20	$p_{mhl}=55$	0.004	
<i>k</i>	20	$p_{me}=25$	<i>0.005</i>	
k	20	$p_{me}=30$		0.006
<i>m</i>	20	$p_{mb}=5$	<i>0.005</i>	
m	20	$p_{mb}=4$		0.009
o	15	$n_e=8$		0.055
<i>o</i>	20	$n_e=8$	<i>0.005</i>	

1020

1021

1022

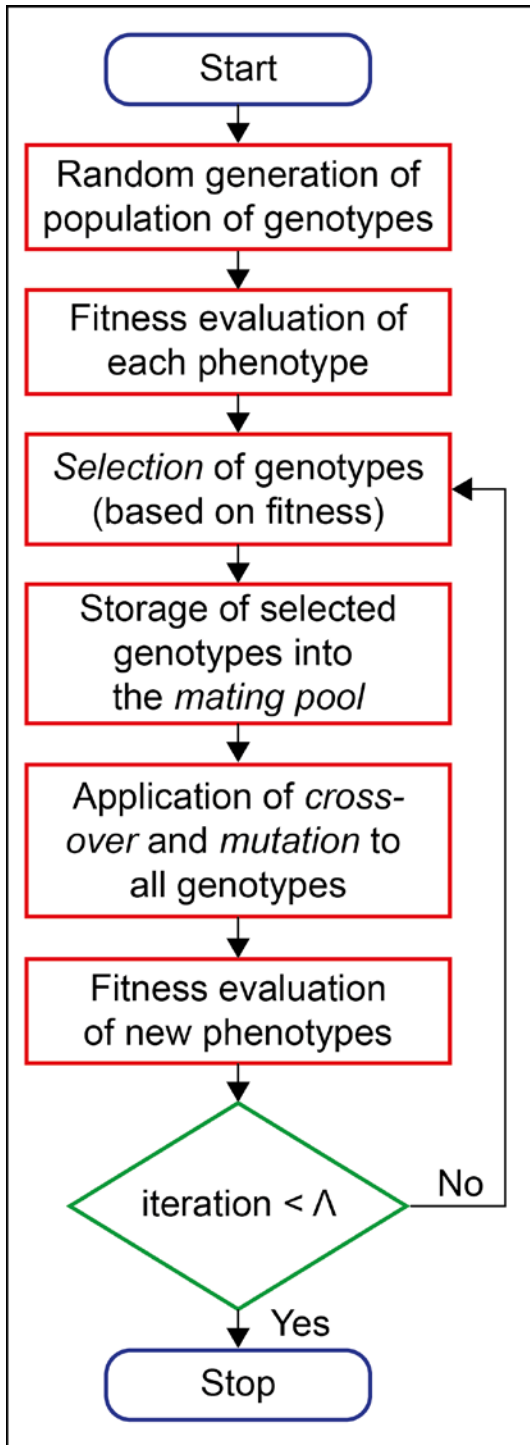
Figure 1. Scheme of the calibration procedure of the model GA^{SAKe} .



1023
1024

1025

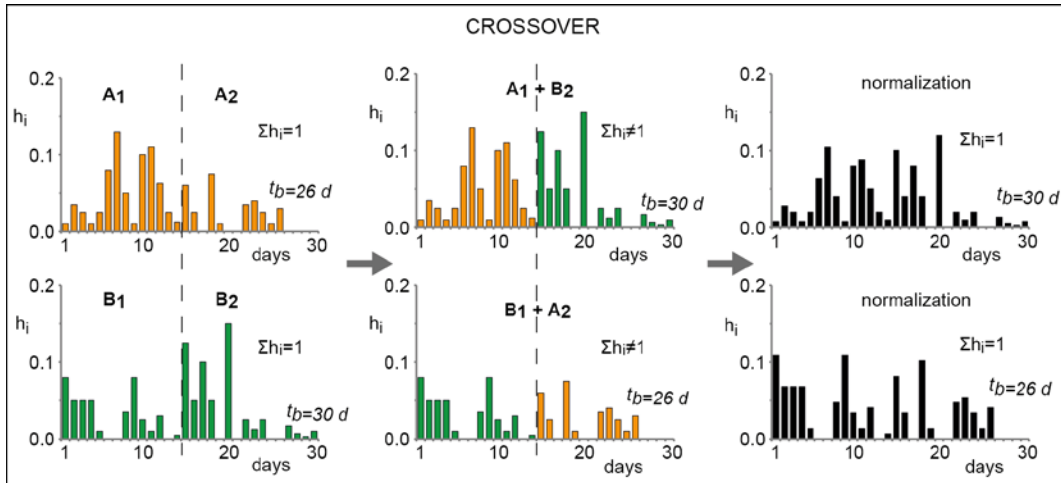
Figure 2. Scheme of the adopted Genetic Algorithm.



1026
1027

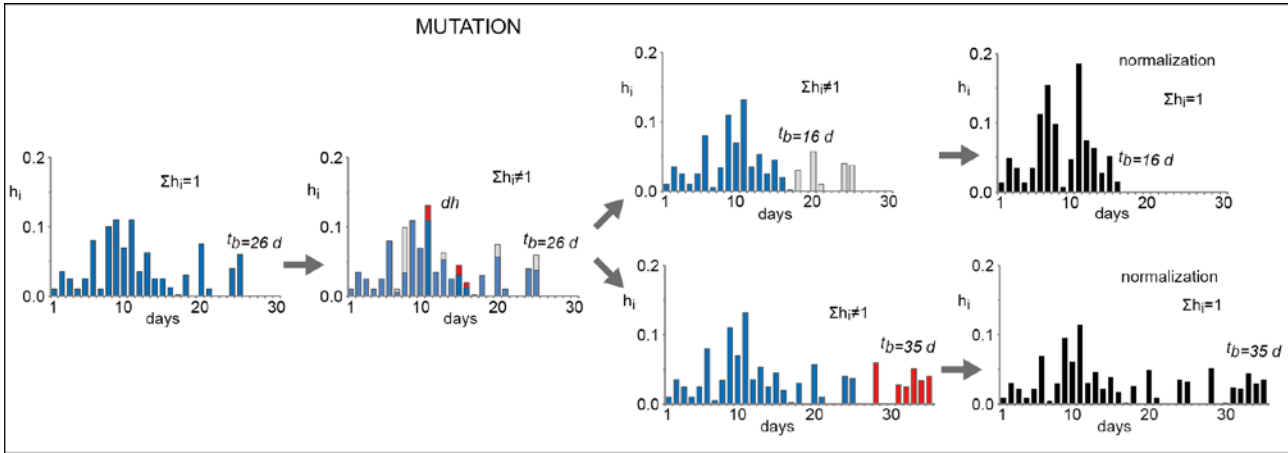
1028
1029

Figure 3. Example of crossover. The genetic codes of the parents (elements in orange and green) are first mixed; then, the children are normalized (black elements) to ensure validity of equation 2.



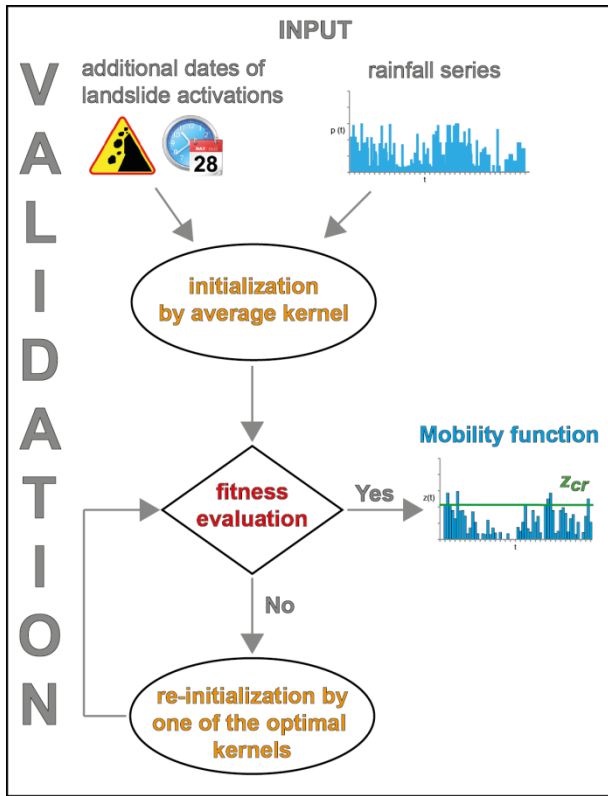
1030
1031

1032 **Figure 4.** Examples of mutation. On the left, the genetic code of the parent individual (elements in blue). In the second
 1033 histogram, mutation is applied to some elements of the parent (in red, added amounts; in grey, subtracted amounts).
 1034 Then, the base time can either be decreased (upper sequence) or increased (lower sequence). Finally, the children is
 1035 normalized (black elements) to ensure validity of equation 2.



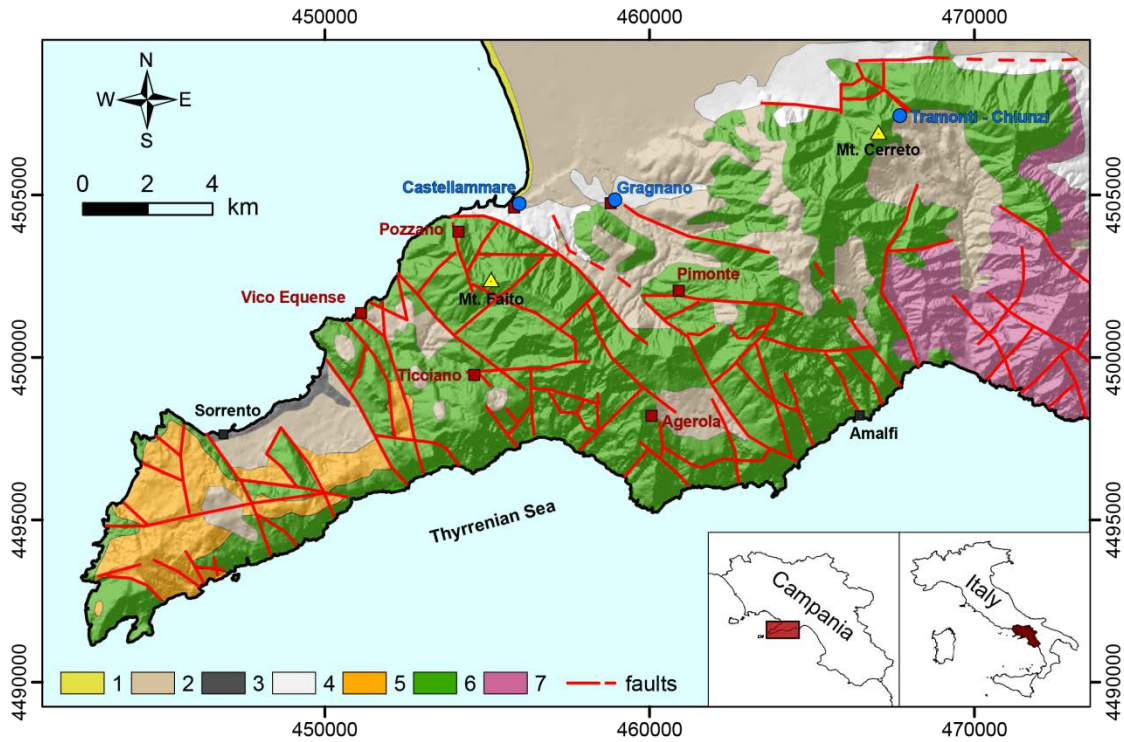
1036
 1037

1038 **Figure 5.** Scheme of the validation procedure of the model GA_{SAKe} .



1039
1040

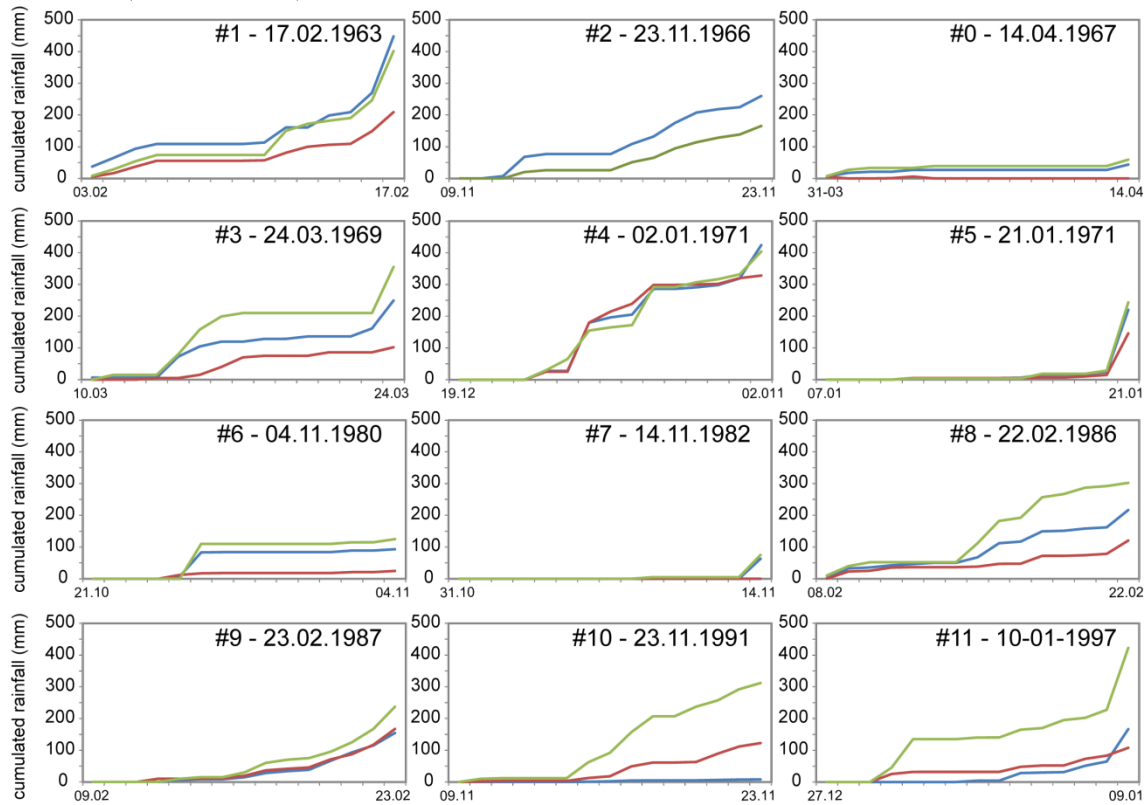
1041 **Figure 6.** Geological map of the Sorrento Peninsula (after Di Crescenzo and Santo, 1999, mod.). Key: 1) beach deposit
 1042 (Holocene); 2) pyroclastic fall deposit (Late Pleistocene-Holocene); 3) Campanian ignimbrite (Late Pleistocene); 4)
 1043 detrital alluvial deposit (Pleistocene); 5) flysch deposit (Miocene); 6) limestone (Mesozoic); 7) dolomitic limestone
 1044 (Mesozoic). Red squares mark sites affected by shallow landslide activations; blue circles, the rain gauges; black
 1045 squares, the main localities; yellow triangles, the highest mountain peaks.



1046
 1047

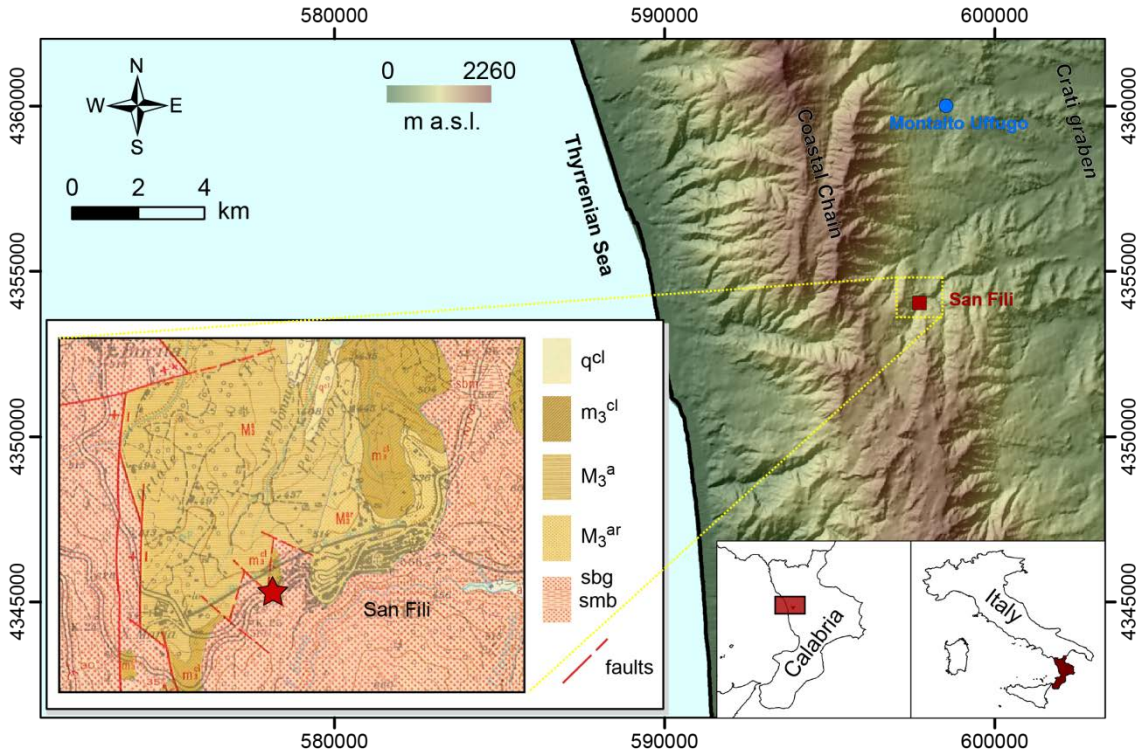
1048
1049
1050

Figure 7. Cumulative daily rainfall (in mm) during the 14 days preceding landslide occurrences. Key: in blu, red, and green = values from the Tramonti, Castellammare, and Tramonti-Chiunzi rain gauges, respectively. Numbers refer to id. in Table 1 (cf. first column).



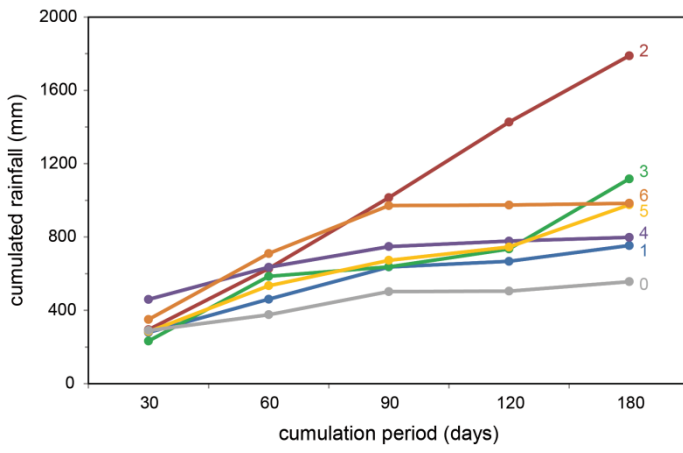
1051
1052

1053 **Figure 8.** Location of the study area (red square: San Fili village; blue circle: Montalto Uffugo rain gauge). On bottom
 1054 left, an extract from the geological map of Calabria (CASMEZ, 1967). Key: sbg) gneiss and biotitic schist with garnet
 1055 (Palaeozoic); sbm) schist including abundant granite and pegmatite veins, forming migmatite zones (Palaeozoic); M_3^{ar}
 1056 arenite and silt with calcarenite (Late Miocene); M_3^a) marly clay with arenite and marls (Late Miocene); m_3^{cl}) reddish
 1057 conglomerate with arenite (Late Miocene); q^{cl}) loose conglomerate of ancient fluvial terraces (Pleistocene). The site
 1058 affected by the Uncino landslide is marked by a red star.



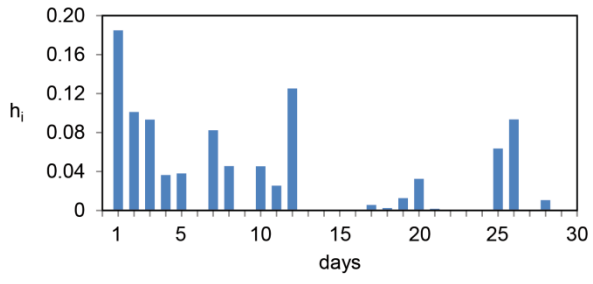
1059
 1060

1061 **Figure 9.** Cumulative daily rainfall (in mm) from 30 to 180 days before landslide occurrences (Montalto Uffugo
1062 gauge). Numbers refer to identification number (#) in Table 2 (cf. first column).



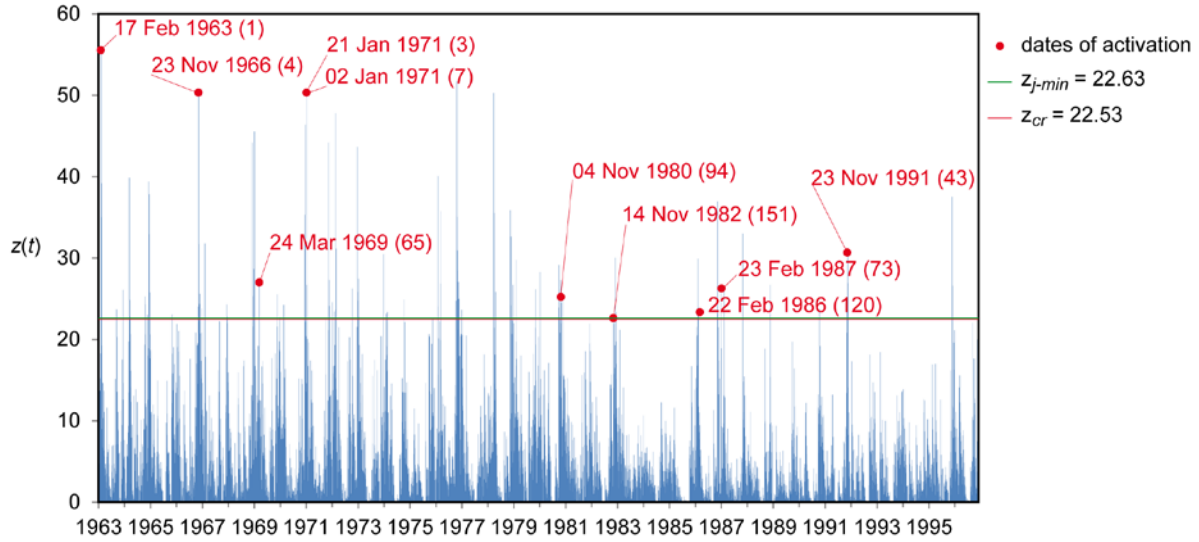
1063
1064

1065 **Figure 10.** Sorrento Peninsula case study. Average kernel obtained from the best 100 filter functions.



1066
1067

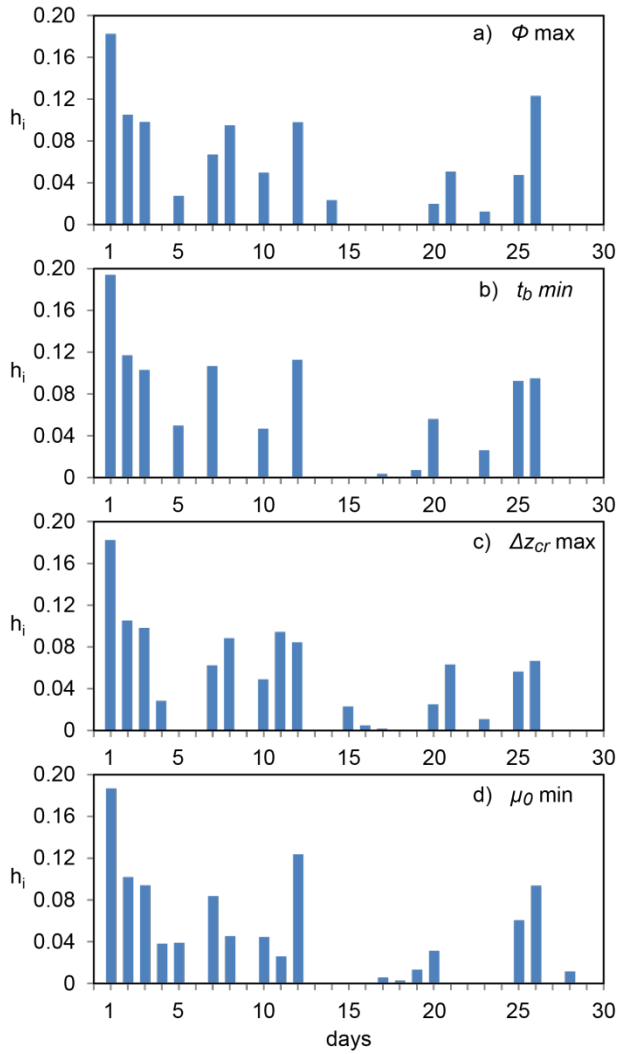
1068 **Figure 11.** Sorrento Peninsula case study. Mobility function, $z(t)$, of the average kernel. The red line ($z_{cr} = 22.53$) shows
 1069 the maximum value of the mobility function (critical condition) that is unrelated to known landslide activations. The
 1070 green line ($z_{j-min} = 22.63$) – almost overlapping with the red line in this case – shows the minimum value of the mobility
 1071 function related to known landslide activations. When the mobility function exceeds the threshold marked by the red
 1072 line, landslide activation may occur. The red dots represent the maxima of the mobility function corresponding to the
 1073 dates of landslide activation considered for calibration.



1074
1075

1076
1077

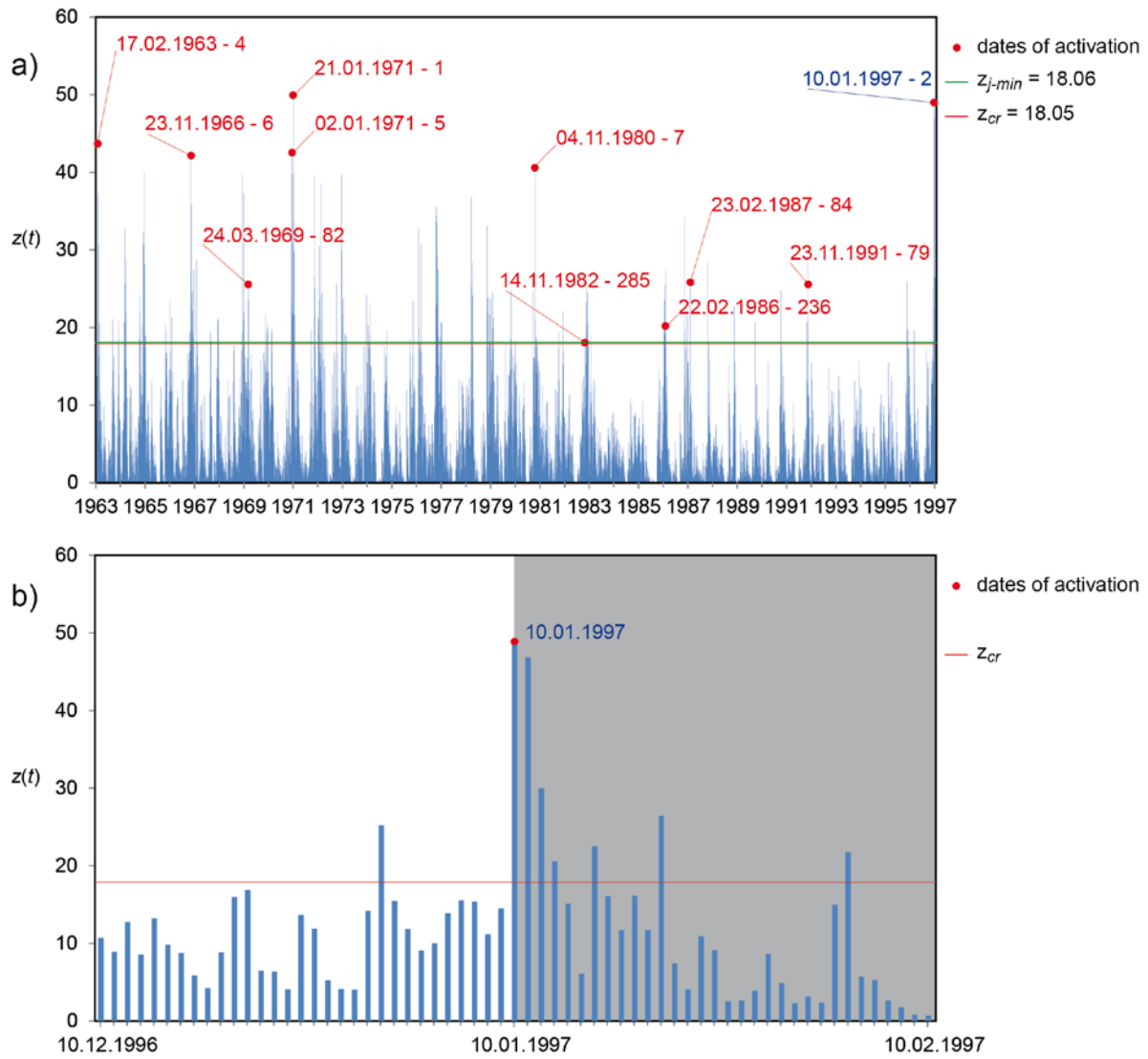
Figure 12. Sorrento Peninsula case study. Kernels providing (a) the best fitness ($\Phi_{max} = 0.807$), (b) the minimum base time $t_b \min$ (26 days), (c) the $\Delta z_{cr} \max$ (0.00801), and (d) the minimum first order momentum, $\mu_0 \min$ (9.460).



1078
1079

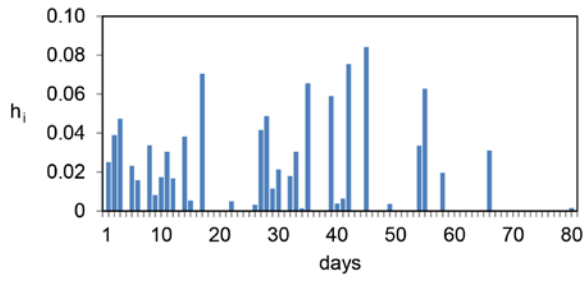
1080
1081
1082

Figure 13. Sorrento Peninsula case study. a) Validation of the average kernel against the #11 event. b) Particular of Fig.13a, limited to the period $\pm t_b$, including the date of validation. Key as in Fig.11. The blue label indicates the date of validation. Grey background marks the period after the event that may be employed for re-calibration.



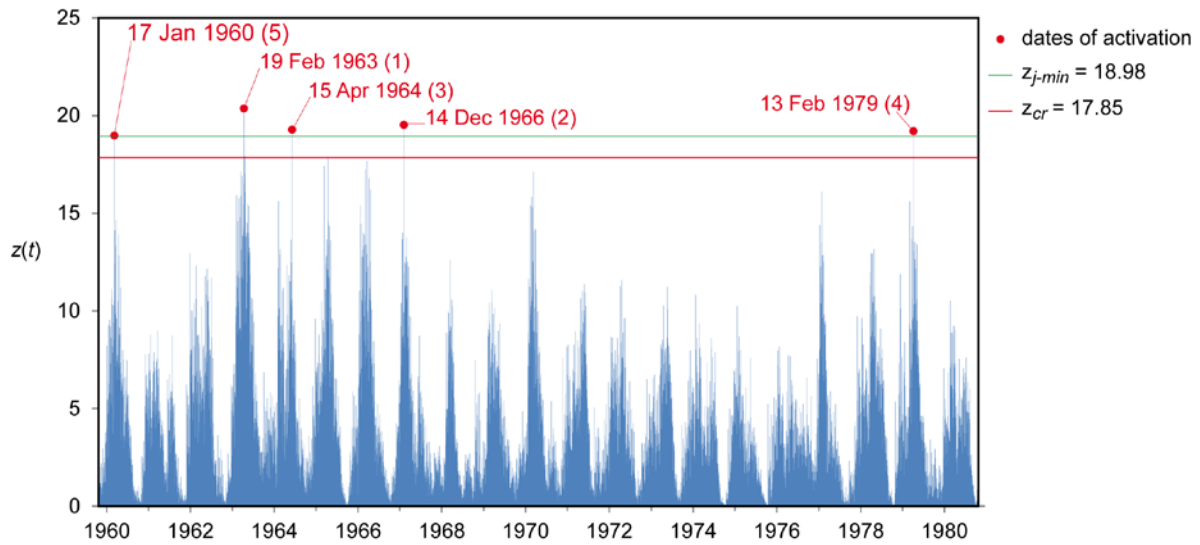
1083
1084

1085 **Figure 14.** Uncino landslide case study. Average kernel obtained from the best 100 filter functions.

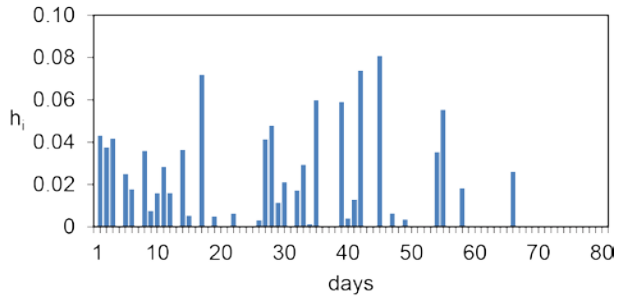


1086
1087

1088 **Figure 15.** Uncino landslide case study. Mobility function, $z(t)$, of the average kernel. The red line ($z_{cr} = 17.85$) shows
1089 the maximum value of the mobility function (critical condition) that is unrelated to known activations. The green line
1090 ($z_{j-min} = 18.98$) shows the minimum value of the mobility function related to known activations. When the mobility
1091 function exceeds the threshold marked by the red line, landslide activation may occur. The red dots represent the
1092 maxima of the mobility function corresponding to dates of landslide activation considered for calibration.

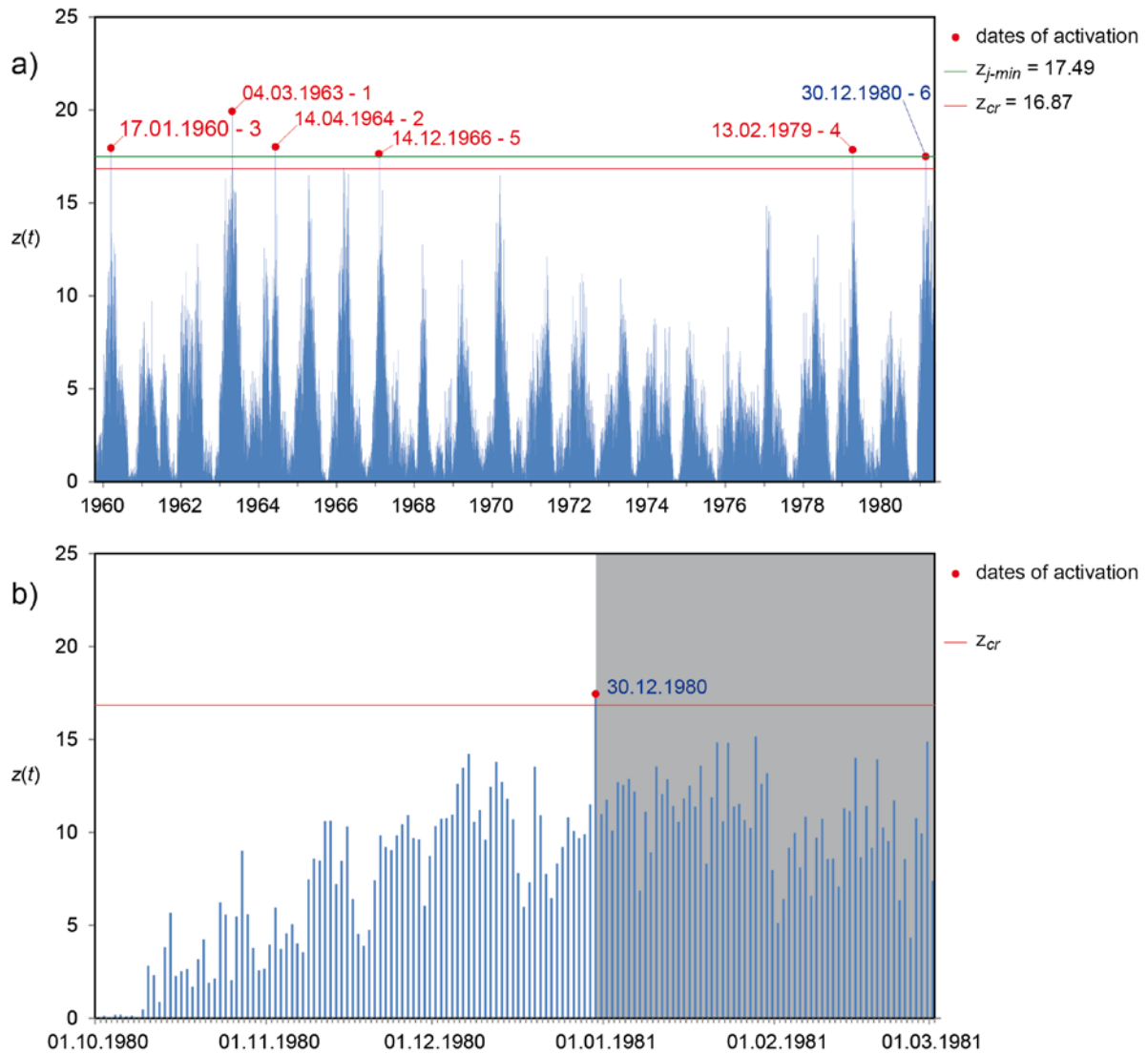


1095 **Figure 16.** Uncino landslide case study. Kernel providing the best fitness.



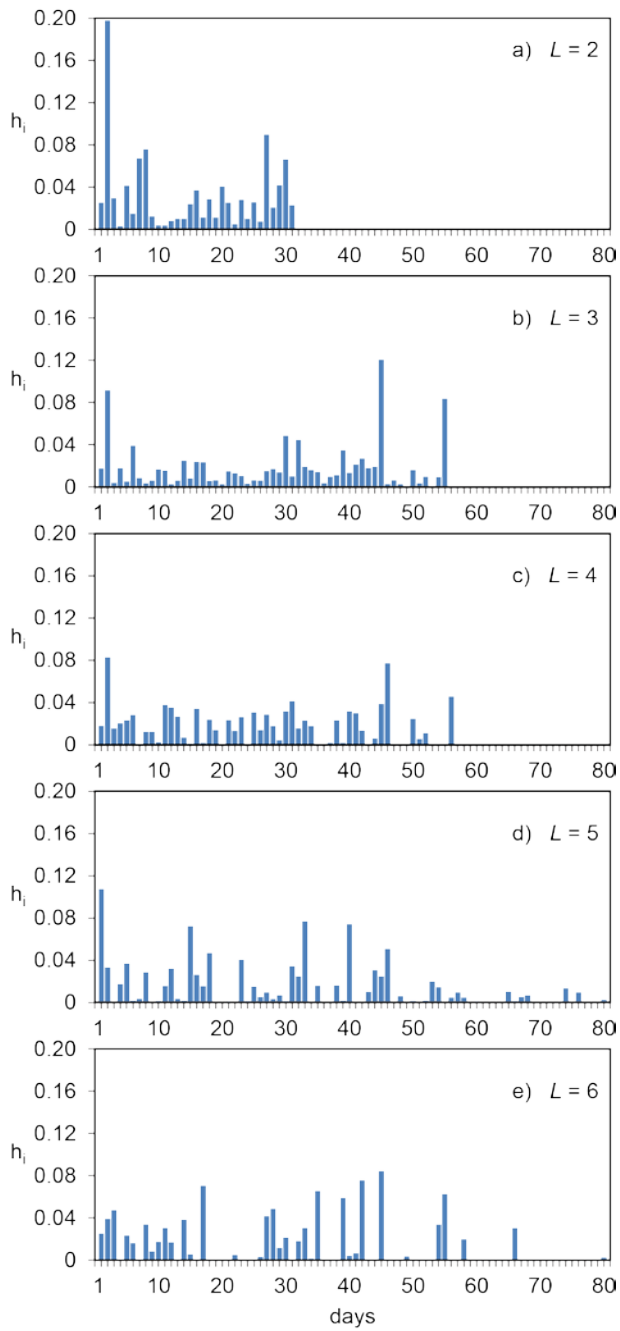
1096
1097

1098 **Figure 17.** Uncino landslide case study. a) Validation of the average kernel against the #6 event. b) Particular of
 1099 Fig.17a, limited to the period $\pm t_b$ including the date of validation. Key as in Fig. 15. The blue label indicates the date of
 1100 validation. Grey background marks the period after the event that may be employed for re-calibration.



1101
 1102

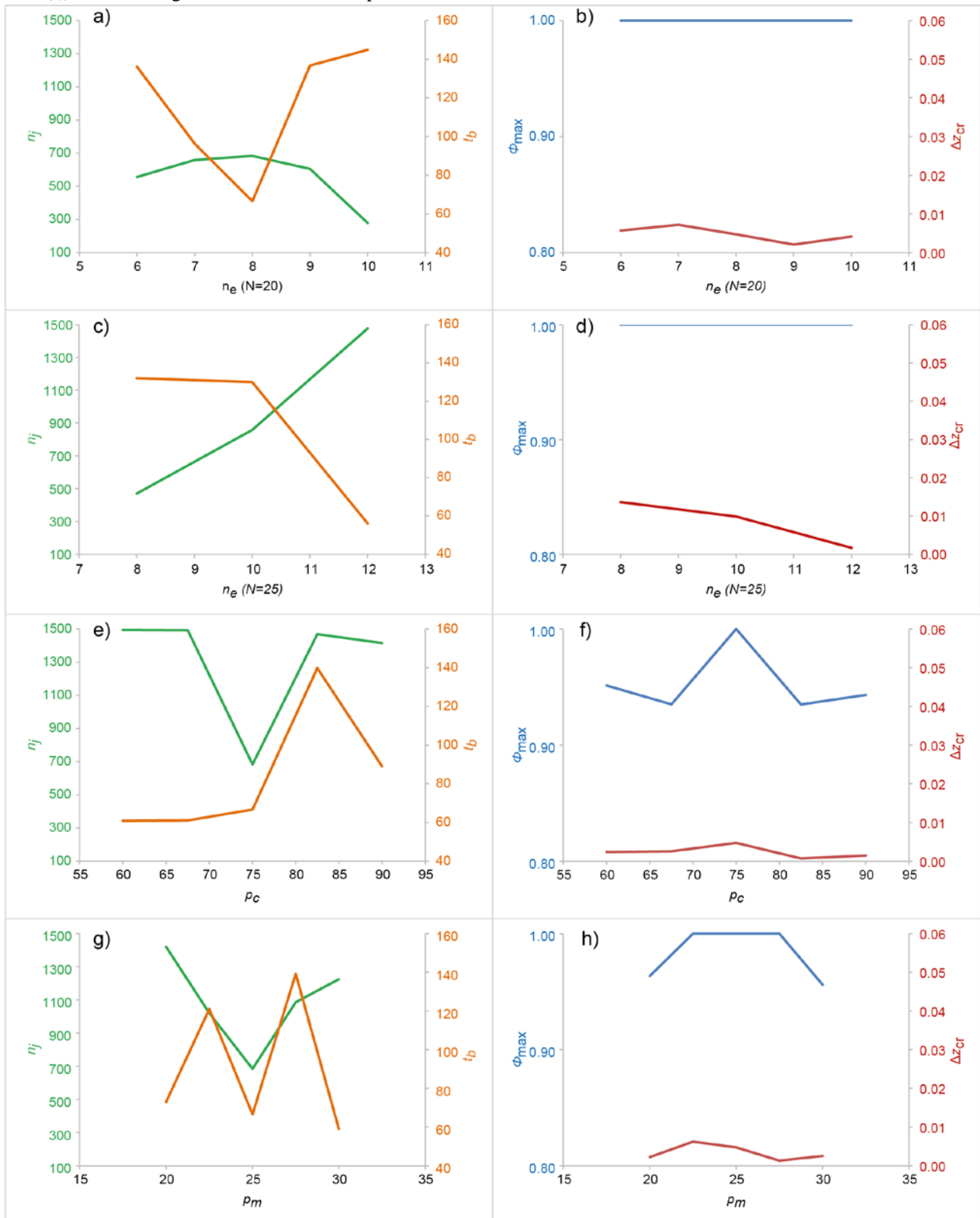
1103 **Figure 18.** Uncino landslide case study. Average kernels obtained in calibration against the 2, 3, 4, 5, and 6 dates of
1104 activation.



1105
1106

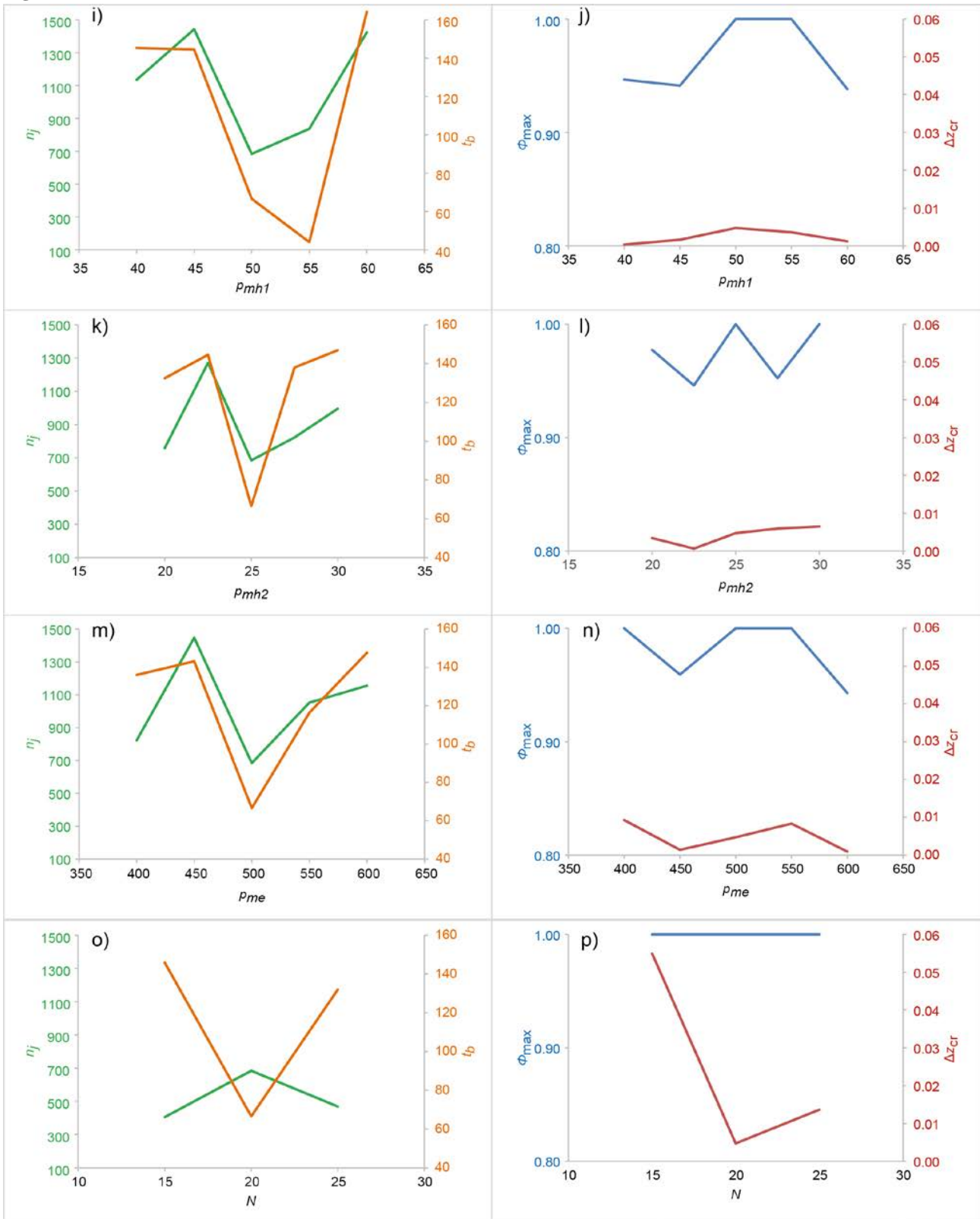
1107
1108

Figure 19. Maximum fitness (Φ_{max}), safety margin (Δz_{cr}), number (n_i) of iterations needed to first reach Φ_{max} , and base time (t_b) of the average kernel, based on GA parameters listed in Table 8.



1109
1110

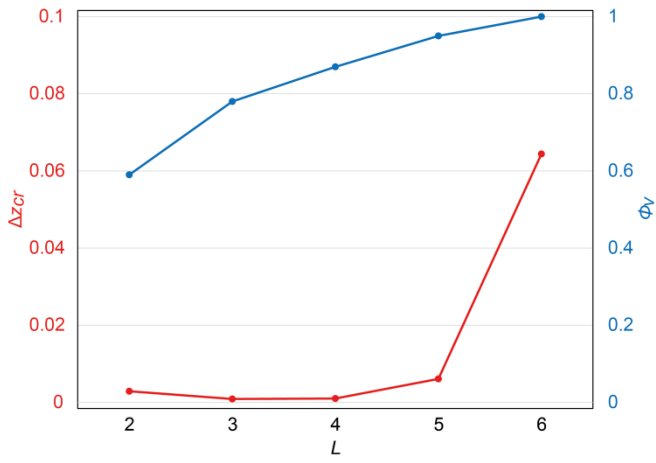
1111 **Figure 19**



1112

1113

1114 **Figure 20.** Uncino landslide case study. Results of progressive calibration. Variation of Δz_{cr} and Φ_v for L increasing
1115 from 2 to 6.



1116
1117